Reports on Progress in Physics

REVIEW

Many-body near-field radiative heat transfer: methods, functionalities and applications

To cite this article: Jinlin Song *et al* 2021 *Rep. Prog. Phys.* **84** 036501

IOP Publishing Reports on Progress in Physics
Rep. Prog. Phys. **84** (2021) 036501 (24pp) https://doi.org/10.1088/1361-6633/abe52b

Review

Many-body near-field radiative heat transfer: methods, functionalities and applications

Jinlin Song[1,2], Qiang Cheng[2,*], Bo Zhang[2], Lu Lu[2], Xinping Zhou[3], Zixue Luo[2] and Run Hu[2,*]

[1] School of Electrical and Information Engineering, Wuhan Institute of Technology, Wuhan 430025, Hubei, People's Republic of China
[2] State Key Laboratory of Coal Combustion, School of Energy and Power Engineering, Huazhong University of Science and Technology, Wuhan 430074, Hubei, People's Republic of China
[3] School of Mechanical Science and Engineering, Huazhong University of Science and Technology, Wuhan 430074, Hubei, People's Republic of China

E-mail: chengqiang@mail.hust.edu.cn and hurun@hust.edu.cn

Received 6 August 2020, revised 2 February 2021
Accepted for publication 10 February 2021
Published 4 March 2021

Abstract

Near-field radiative heat transfer (NFRHT) governed by evanescent waves, provides a platform to thoroughly understand the transport behavior of nonradiative photons, and also has great potential in high-efficiency energy harvesting and thermal management at the nanoscale. It is more usual in nature that objects participate in heat transfer process in many-body form rather than the frequently-considered two-body scenarios, and the inborn mutual interactions among objects are important to be understood and utilized for practical applications. The last decade has witnessed considerable achievements on many-body NFRHT, ranging from the establishment of different calculation methods to various unprecedented heat transport phenomena that are distinct from two-body systems. In this invited review, we introduce concisely the basic physics of NFRHT, lay out various theoretical methods to deal with many-body NFRHT, and highlight unique functionalities realized in many-body systems and the resulting applications. At last, the key challenges and opportunities of many-body NFRHT in terms of fundamental physics, experimental validations, and potential applications are outlined and discussed.

Keywords: near-field radiative heat transfer, many-body system, thermal functionality, theoretical method

(Some figures may appear in colour only in the online journal)

* Authors to whom any correspondence should be addressed.
'Corresponding Editor Professor Masud Mansuripur'.

1. Introduction

Radiative heat transfer (RHT) is a ubiquitous physical phenomenon between arbitrary objects at nonzero absolute temperatures, ranging from the Sun, industrial boiler, incandescent bulb, to nanoantenna [1, 2]. The fundamental physics behind RHT has been well understood over a century from the introduction of Planck's law for describing the radiation spectrum of an ideal black-body object at a given temperature, which has been universally recognized as the origin of quantum mechanics [3, 4]. Planck's law then leads to the famous Stefan–Boltzmann law for radiated power exchanged of $\sigma\left(T_1^4 - T_2^4\right)$ between two black-body objects at different temperatures T_1 and T_2 where σ is the Stefan–Boltzmann constant, capping the theoretical radiative heat flux between real materials in the far-field regime. However, Planck's law is derived using the geometric optical method based on the assumption that the dimension and separation distance are much larger than the characteristic wavelength of thermal radiation λ_{th} (7.63 μm at 300 K), so it is not adaptable when the separation distance between the objects is less than λ_{th}, i.e. in the near-field regime. In 1971, Polder and Van Hove [5] computed the radiative heat flux between two closely spaced chromium half spaces based on Rytov's fluctuational electrodynamics (FE) [6]. They theoretically predicted that evanescent waves dominate the RHT at the nanoscale, i.e. near-field radiative heat transfer (NFRHT), and make the heat flux greatly surpass the corresponding value in the far-field regime. Evanescent waves, which exist inside the optically rarer medium, decay exponentially away from the interface and carry no energy in the direction normal to the interface. But, if two optically denser media are brought into close proximity with the gap distance being smaller than λ_{th}, energy can be transmitted between them, even though the total internal reflection occurs when the angle of incidence is larger than the critical angle. This phenomenon is called photon tunneling, which can also be regarded as the coupling of two oppositely decaying evanescent waves. In recent decades, with the help of the rapid development of nanoscale fabrication and measurement technologies, heat transport governed by evanescent waves at the nanoscale was experimentally demonstrated in terms of materials and configurations [7–31]. It has been demonstrated that the evanescent waves enable several orders-of-magnitude enhancement of heat flux over the black-body limit at room temperature. This convincing evidence sparks renewed interest in the study on NFRHT to pursue the huge potential in high-efficiency energy conversion and thermal management at the nanoscale, including thermal microscopy, heat-assisted magnetic recording, thermophotovoltaics, and thermal rectification [9–16, 18, 20, 21, 27, 28, 32–39]. Meanwhile, an in-depth investigation on NFRHT also facilitates the further physical comprehension on the photon propagation especially for evanescent waves.

At the beginning, the investigations on NFRHT focus on two-body systems where only two objects participate in heat transfer. In this case, there only exists a rather small transfer coefficient that stands for a small photon tunneling probability, associated with the number of tunneling photons, for each channel of evanescent waves. Meanwhile, the total number of channels contributing to the heat transfer shows strong dependence on the transverse wavevector. Even though these deficiencies can be alleviated by taking advantage of materials supporting extraordinary photon propagation modes (e.g. hyperbolic modes, surface polaritons, magnetic polaritons, epsilon near-zero effects, etc [40–71]) to obtain large transfer coefficients and photon tunneling modes supporting high transverse wavevectors (i.e. high-k modes), they still limit the fundamental RHT between two objects, and conflict with the goal of a stronger heat flux which is more desired for real applications. The last decade witnessed the influential achievements of advances in theoretical physics on NFRHT within many-body systems with at least three objects participating in heat transport which shows great enhancement of RHT compared to that in two-body systems. For example, intercalating a planar plate between two plates allows for passive amplification of heat flux even without introducing any extra thermal sources [72]. The mutual interactions within a collection of individual objects enable NFRHT to show distinct transport mechanisms in stark contrast to two-body systems, and also endows heat transfer with high tunability by regulating the optical properties of intermediated ones, e.g. using insulator–metal transition (IMT) materials. Very recently, using many-body interactions, the remarkable modulation of RHT between two coplanar membranes has been experimentally demonstrated [73]. Furthermore, the magneto-optical (MO) effects-induced radiative heat transport, together with many-body mutual interactions, generates unforeseen physics in terms of NFRHT which takes NFRHT to a new level [74–77]. Many-body problems are also indispensable to constitute the theoretical frameworks of numerous branches of physics, including condensed matter physics, atomic physics and so on. Therefore, investigations on many-body NFRHT are significant to the in-depth comprehensions of nonradiative photon heat transport from a broader perspective, and also pave the way to new functionalities for high-performance energy utilization and thermal management at the nanoscale. However, as far as we are concerned, there are not a comprehensive review paper that summarizes these significant progresses on many-body NFRHT in terms of the theories, functionalities, and applications, although there has existed a review article [78] in the field of RHT, including NFRHT, the control of thermal emission and far-field RHT.

To summarize the progress and outline the future directions, we present a summary of the state-of-the-art advances on NFRHT in many-body systems in this invited review. Firstly, we introduce the theoretical methods to deal with many-body NFRHT in terms of geometries and optical properties. Then we emphasize on the unique functionalities and their resulting applications in many-body systems, followed by an open discussion on the challenges and future directions. This topical review paper is expected to provide an overview of the fundamental physics, emerging functionalities, and enabling applications of many-body NFRHT for the heat transfer, nanophotonic engineering, and near-field physics community,

and trigger inspiration and discussion on this emerging field in extensive and intensive ways.

2. Theoretical methods

NFRHT, in essence, is an electromagnetic (EM) wave scattering problem, and is consequently strongly material- and geometry-dependent, leading to different treatments concerning various configurations. To theoretically quantify NFRHT in many-body systems, there are in general two kinds of fundamental framework thus far. The first one is the FE formalism by combining the Maxwell equations with the fluctuation–dissipation theorem (FDT). This kind of framework is more popular, and can further be divided into several specific methods to conveniently describe the radiated EM fields according to the dimensions, shapes and optical properties of the constituent objects. The second one, mainly for ordered particle systems (especially for the chain of nanoparticles) supporting resonant modes (eigenstates), is based on the kinetic theory (KT) approach combined with the Boltzmann transport equation (BTE) to solve the distribution function of thermal photons. We here briefly introduce these EM methodologies to address NFRHT in many-body systems for better understanding.

2.1. Fluctuational electrodynamics

In analogy with the Langevin model for Brownian motion which introduces a random force as the source to derive the statistical properties of their random motion by the dynamical equations of the particles [79], Rytov modeled fluctuating EM fields as the external random source to describe the random thermally driven EM fields by Maxwell equations, known as FE [6]. The core idea is that, charges, e.g. electrons and ions, suffer a random thermal motion for any material (globally neutral) above 0 K, leading to the formation of fluctuating fields which radiate an EM field. Assuming that all materials are non-magnetic ($\mu = 1$), Maxwell equations lead to the vector Helmholtz wave equations governing the transport of EM waves which can be written as

$$\nabla \times \nabla \times \mathbf{E}(\mathbf{r},\omega) - \varepsilon(\omega) k_0^2 \mathbf{E}(\mathbf{r},\omega) = i\omega\mu_0 \mathbf{J}(\mathbf{r},\omega), \quad (1)$$

$$\nabla \times \nabla \times \mathbf{H}(\mathbf{r},\omega) - \varepsilon(\omega) k_0^2 \mathbf{H}(\mathbf{r},\omega) = \nabla \times \mathbf{J}(\mathbf{r},\omega), \quad (2)$$

where $\mathbf{E}$ and $\mathbf{H}$ are the electric and magnetic field vectors, ε is the permittivity, k_0 is the wavevector in vacuum and μ_0 is the vacuum permeability. Rather than EM fields modeled as thermal sources by Rytov, the fluctuating electric currents $\mathbf{J}$ are used here which are associated with the statistical properties of random thermal sources of the objects by the FDT:

$$\left\langle J_\beta(\mathbf{r},\omega) J^*_{\beta'}\left(\mathbf{r}',\omega'\right)\right\rangle = \frac{4}{\pi}\omega\varepsilon_0 \mathrm{Im}\left[\varepsilon(\omega)\right]\Theta(\omega,T)\delta_{\beta\beta'} \times \delta\left(\mathbf{r}-\mathbf{r}'\right)\delta\left(\omega-\omega'\right), \quad (3)$$

where $\beta = x, y, z$ labels the Cartesian coordinates with the asterisk denoting complex conjugation, ε_0 is the vacuum permittivity, and $\Theta(\omega,T) = \frac{\hbar\omega}{\exp(\hbar\omega/k_B T)-1}$ refers to the mean energy of a harmonic oscillator in thermal equilibrium excluding the zero-point contribution $\hbar\omega/2$ which does not affect the net radiation heat flux and where $\hbar$ is the reduced Planck constant and k_B is the Boltzmann constant [80]. The Kronecker delta $\delta_{\beta\beta'}$ denotes no cross coupling between currents in orthogonal directions, while the Dirac delta functions $\delta\left(\mathbf{r}-\mathbf{r}'\right)$ and $\delta\left(\omega-\omega'\right)$ translate the assumption of locality and stationarity in the media. The factor of 4 is included to be consistent with the conventional definitions of the spectral energy density, since only positive frequencies are subsequently considered. Then, with the help of Green functions to link the source currents and the thermally radiated EM fields together with the proper boundary conditions, the thermally excited heat flux (energy flow per unit time per unit area) satisfying the translational invariance, can be directly obtained by the integration of the ensemble-averaged Poynting vector

$$\langle \mathbf{S}(\mathbf{r},\omega)\rangle = \frac{1}{2}\left\langle \mathrm{Re}\left[\mathbf{E}(\mathbf{r},\omega)\times\mathbf{H}^*(\mathbf{r},\omega)\right]\right\rangle, \quad (4)$$

over the whole frequency and the whole region of the receiver. According to the complexity of the system in terms of materials and geometries, the fundamental FE having the ability to deal with many-body systems can be categorized into several analytical and numerical methods as follows.

2.1.1. Analytical formalism. The analytical formalism takes advantage of the Green functions which accurately describe the correlation between all sources and resultant fields to derive the explicit formulae for calculating NFRHT, whereas the Green functions are difficult to obtain for complicated configurations. Therefore, this method is only suitable for highly symmetric geometries including dipoles, spheres, cylinders and 2D planar or periodic structures [72, 81–85]. For dielectric dipolar nano-objects (e.g. nanoparticles, nanodisks) that can be regarded as electric dipoles having electric polarizability α^E to describe the fluctuating currents when their characteristic sizes are much smaller than λ_{th}, the FDT in terms of the fluctuating electric dipole moment $\mathbf{p}$ of each object instead of its electric current $\mathbf{J}$ used in equation (3) is employed based on the dipolar approximation, which reads [86]

$$\left\langle p_{j,\beta}(\omega) p^*_{j',\beta'}\left(\omega'\right)\right\rangle = 2\frac{\varepsilon_0}{\omega}\Theta(\omega,T)\,\mathrm{Im}\left(\alpha_j^E\right)\delta_{jj'}\delta_{\beta\beta'}\delta\left(\omega-\omega'\right). \quad (5)$$

The dipole moment $\mathbf{p}$ of a particle is the summation of the thermally fluctuated part $\mathbf{p}^{\mathrm{fluc}}$ (from its thermal fluctuations) and field-induced part $\mathbf{p}^{\mathrm{ind}}$ (from other particles' fluctuations), i.e. $\mathbf{p} = \mathbf{p}^{\mathrm{fluc}} + \mathbf{p}^{\mathrm{ind}}$. The field-induced dipole moment on particle j can be obtained by superposing the fields radiated by all the other particles which reads

$$\mathbf{p}_j^{\mathrm{ind}} = \varepsilon_0\alpha_j \sum_{k\neq j}\mathbf{E}_{jk}. \quad (6)$$

The electric field at the frequency ω and position r_j generated by the fluctuating electric dipole moment $\mathbf{p}_k^{\mathrm{fluc}}$ of particle k at the position r_k is expressed as

$$\mathbf{E}_{jk} = \omega^2\mu_0\hat{\boldsymbol{G}}_{jk}\mathbf{p}_k^{\mathrm{fluc}}, \quad (7)$$

where $\hat{\boldsymbol{G}}_{jk} \equiv \hat{\boldsymbol{G}}\left(r_j, r_k, \omega\right)$ denotes the dyadic Green tensor between the particles j and k inside the system for brevity. The free space Green function $\hat{\boldsymbol{G}}^0_{jk}$ is written as

$$\hat{\boldsymbol{G}}^0_{jk} = \frac{\mathrm{e}^{\mathrm{i}k_0 r}}{4\pi r_{jk}} \left[\left(1 - \frac{1}{\left(k_0 r_{jk}\right)^2} + \frac{i}{k_0 r_{jk}} \right) \hat{1} - \left(1 - \frac{3}{\left(k_0 r_{jk}\right)^2} + \frac{3i}{k_0 r_{jk}} \right) \hat{\boldsymbol{r}}_{jk} \otimes \hat{\boldsymbol{r}}_{jk} \right], \tag{8}$$

where the unit tensor $\hat{\boldsymbol{r}}_{jk} = \mathbf{r}_{jk}/r_{jk}$ being the vector linking the center of particles j and k. $r_{jk} = |\mathbf{r}_{jk}|$and $\hat{1}$ is the unit dyadic tensor. $\hat{\boldsymbol{G}}_{jk}$ can be directly obtained from the $\hat{\boldsymbol{G}}^0_{jk}$ to take into the mutual interactions of all particles, and thus have explicit expressions in tensor form. Then, using $\mathbf{p}_j^{\mathrm{ind}}$ and $\mathbf{E}_{jk}$ the FDT in equation (5), the power dissipated within particle j from particle k in such a many-body system, which is the part subtracting the scattering part from the whole extinction and can be expressed as

$$\mathcal{P}_{k\to j} = 3\int_0^\infty \frac{\mathrm{d}\omega}{2\pi} \Theta\left(\omega, T_k\right) \mathcal{T}_{k\to j}\left(\omega\right), \tag{9}$$

where $\mathcal{T}_{k\to j}$ denotes the energy transfer coefficient (ETC) from particle k to particle j. Then, the interparticle heat flux can be given by $\varphi_{jk} = \mathcal{P}_{j\to k} - \mathcal{P}_{k\to j}$. This self-consistent method can be extended to systems consisting of anisotropic materials with α^{E} in the anisotropic tensor form, and also can be generalized to consider the far-field radiative losses towards the surrounding medium and the self-emission of particles [87, 88]. Radiative corrections [89] based on the energy balance are at times utilized for accurate calculation for anisotropic nanoparticles, although they have little influence in most cases. For a metallic nanoparticle, it introduces magnetic dipole moment $\mathbf{m}$ due to the eddy current, which gives a significant contribution to absorption especially in the extremely near field [90]. If the many-body system simultaneously has dielectric and metallic particles, the coupled electric and magnetic dipole approach instead of treating them separately should be considered due to the existence of the coupling of electric and magnetic interactions [91].

With regard to many-body systems with planar geometry, the closed-form analytical formula for heat flux can be given in a Landauer-type using the exact scattering theory [85]. In this scenario, many-body scattering coefficients are required to describe the mutual interactions of different bodies at the same time. In an N-body system, the scattering coefficients are built based on the single-body forward and backward reflection and transmission coefficients, i.e. ρ_j and τ_j $(j = 1, \ldots, N)$, depending only on the modulus of the wavevector due to the cylindrical symmetry. With regard to a block of consecutive bodies within this system, its reflection and transmission coefficients, representing the analogues of ρ_j and τ_j for a single body, consider the multiple reflections within the cavity and transmission through this block. Then, with the help of the electric field coefficients L which relates source fields $\mathcal{E}$ to total fields E in a given region of the system by $E = \sum L\mathcal{E}$ in terms of sources, regions and directions (see the details in [85]), the ETCs within the system can be explicitly determined to deal with many-body effects. It has to been noted that, for the simplest case, i.e. a three-plate system with $N = 3$ and separation distance d, the intermediate block reduces to a single plate (indexed by 2 here), and the heat flux between the terminal plates (indexed by 1 and 3) can be simply expressed by the following equation,

$$\varphi = \frac{1}{\pi^2}\int_0^\infty \int_{\beta>k_0}^\infty \beta\,\mathrm{d}\beta\,\mathrm{d}\omega \left\{ \left[\Theta\left(\omega, T_1\right) - \Theta\left(\omega, T_2\right)\right] \mathcal{T}_{12} + \left[\Theta\left(\omega, T_2\right) - \Theta\left(\omega, T_3\right)\right] \mathcal{T}_{23} \right\}, \tag{10}$$

where β is the parallel component of the wavevector along the interface. $\mathcal{T}_{12} = \frac{4|\tau_2|^2\,\mathrm{Im}(\rho_1)\mathrm{Im}(\rho_3)\mathrm{e}^{4\mathrm{i}k_{z0}d}}{\left|1-\rho_{12}\rho_3\,\mathrm{e}^{2\mathrm{i}k_{z0}d}\right|^2\left|1-\rho_1\rho_2\,\mathrm{e}^{2\mathrm{i}k_{z0}d}\right|^2}$ and $\mathcal{T}_{23} = \frac{4\,\mathrm{Im}(\rho_{12})\mathrm{Im}(\rho_3)\mathrm{e}^{2\mathrm{i}k_{z0}d}}{\left|1-\rho_{12}\rho_3\,\mathrm{e}^{2\mathrm{i}k_{z0}d}\right|^2}$ takes the transmission τ_2 of the plate 2 (the intermediate one) and reflection ρ_{12} of the couple of plates (1, 2) into account to describe the energy transfer in the system. Here, $\rho_{12} = \rho_2 + \frac{\rho_1(\tau_2)^2\,\mathrm{e}^{2\mathrm{i}k_{z0}d}}{1-\rho_1\rho_2\,\mathrm{e}^{2\mathrm{i}k_{z0}d}}$. Using this method, the three-body passive amplification of NFRHT, as well as the heat engine are theoretically predicted [72, 84]. Furthermore, this method can also be extended by using the effective medium theory to approximately describe the optical properties for planar systems consisting of composite materials [81], or by using the semi-analytical rigorous coupled-wave analysis (RCWA) to deal with well-defined periodic structures [82].

2.1.2. Scattering matrix method. For complicated many-body systems, e.g. arbitrarily geometric, optically anisotropic or having a large number of objects, numerical methods are more convenient and sometimes necessary to deal with NFRHT. In light of this point, several theoretical approaches have been proposed, which mainly differ in the aspect of how the analysis is illustrated conceptually and mathematically. The scattering matrix method, which has been employed to compute NFRHT in sphere-plate and multilayered systems [92–94], uses the scattering matrix to link a set of separately incoming and outgoing wave amplitudes with unknown EM fields distributed within the individual objects [95]. Using this method, Krüger and colleagues [96] derived compact and basis-independent trace formulas to compute the heat transfer for arbitrarily shaped many-body systems in the framework of FE. The formulas are completely determined by the scattering operators $\hat{\boldsymbol{T}}$ of individual objects and the free space Green function $\hat{\boldsymbol{G}}^0$. The scattering operator, derived from the Lippmann–Schwinger equation [97], characterizes the scattering behavior through encoding both the geometric and optical properties of the object in it, whereby the magnitude of heat flow absorbed by one object contributed by another object can be recorded. In the presence of a passive nonabsorbing background medium with a characteristic temperature, the Green function $\hat{\boldsymbol{G}}^{\mathrm{b}}$ of the background medium is used instead of $\hat{\boldsymbol{G}}^0$ in the vacuum case to consider the interactions of the objects with the surrounding. The scattering operators $\hat{\boldsymbol{T}}$ and $\hat{\boldsymbol{G}}^{\mathrm{b}}$ are related by $\hat{\boldsymbol{G}} = \hat{\boldsymbol{G}}^{\mathrm{b}} + \hat{\boldsymbol{G}}^{\mathrm{b}}\hat{\boldsymbol{T}}\hat{\boldsymbol{G}}^{\mathrm{b}}$ in this case to describe the Green function of the system [92]. However, this method requires

beforehand computing the scattering matrix for the considered composite consisting of multiple objects with choosing the appropriate partial wave bases for all individual objects, which is nontrivial and needs substantial groundwork. For convenience, Zhu *et al* [98] further developed this method by using a self-consistent scattered field approach. This method only considers the scattering matrix of individual objects instead of the composite such that allows for efficient numerical calculation to avoid excessive preliminary work. It takes all the modes into account so that is not restricted to conditions of dipolar approximation in terms of sizes and distances, and situations, where higher-order modes may have considerable contribution to NFRHT. Furthermore, this method is applicable for nonreciprocal cases, and also allows for studying NFRHT in many-body systems consisting of a large number of objects.

For planar many-body systems with optical anisotropy, Chen *et al* propose a method termed as multilayer electromagnetic solver for heat transfer based on scattering matrix formalism, which provides a stable numerical algorithm to compute the NFRHT, where $\left(\varepsilon_{\beta\beta'}-\varepsilon^{*}_{\beta'\beta}\right)/2i$ is used in the FDT to characterize the optical anisotropy of material [99]. This method directly calculates the Green function to describe the radiated fields from the random thermal sources which is particularly suitable for many-body cases, and then analytically perform the spatial integration over the whole emitting volume instead of evaluating the certain field correlators. In addition, the implementation can further be generalized to deal with periodic structures (2D patterns, including rectangle, circle, ellipse and polygon) by employing RCWA with its standard procedure to describe the radiated EM fields, even though the permittivity tensor of each layer has nonzero off-diagonal elements.

2.1.3. Thermal discrete dipole approximation. To begin with, the thermal discrete dipole approximation (TDDA) is proposed for simulating NFRHT between 3D arbitrarily-shaped objects in two-body systems in the spirit of the well-known discrete-dipole approximation (DDA) [100]. They both solve scattering problems by discretizing each object into volume elements that are sufficiently small to be regarded as electric dipoles, and are expectedly applicable for arbitrary geometries. However, the TDDA uses the thermal fluctuation of dipoles as the thermal source which differs from the DDA that uses incident fields associated with external illumination as the source [101]. In the TDDA, the induced dipole moments in vacuum are related to the total macroscopic electric fields, which read [102]

$$\mathbf{p}_j^{\mathrm{ind}} = k_0^2\alpha_j^0\sum_k \hat{\boldsymbol{G}}_{jk}^0\cdot\mathbf{p}_k, \tag{11}$$

where the summation covers all dipoles, and $\alpha_j^0 = V_j\left(\varepsilon_j-\varepsilon_{\mathrm{b}}\right)$ with V_j being the volume and ε_{b} the permittivity of the background medium. This formula includes the effects of all fields on the dipole moment, together with those generated by its own fluctuating currents, and hence differs from equation (6) where the induced dipole moments are related to the external electric fields. At last, the radiative thermal conductance can be given in the Landauer-like form using the integration of the ETC $\mathcal{T}(\omega)$ including both the near-field and the far-field contributions. The TDDA discretizes each object, like cubes and spheres [101], into multiple cubical sub-volumes, so it can also deal with arbitrary shapes with finite sizes and even optical anisotropy. However, when dealing with many-body systems made of a large number of objects, it requires one to solve linear systems with a large number of unknowns which remarkably increase computational costs due to the difficulty of convergence.

2.1.4. Fluctuating surface-current approach. On the basis of the surface-integral-equation method of classical electromagnetism, the fluctuating surface-current (FSC) approach of thermal radiation was first introduced by Rodriguez *et al* [103, 104] to deal with systems composed of arbitrary geometries even if there is the contribution from the environment. In the FSC approach, the RHT between two objects at temperatures T_1 and T_2, can be written as

$$\varphi = \int_0^\infty \mathrm{d}\omega\left[\Theta(\omega,T_1)-\Theta(\omega,T_2)\right]\mathcal{T}(\omega), \tag{12}$$

where $\mathcal{T}$ is an ensemble-averaged heat flux spectrum. It can be expressed purely in terms of interactions of fictitious unknown electric and magnetic currents located on the surfaces of the objects without the constraint of any wave equation, and reads in the following compact expression

$$\mathcal{T} = \frac{1}{2\pi}\,\mathrm{Tr}\left[(\mathrm{sym}\,G_1)\,W_{21}^{*}\,(\mathrm{sym}\,\mathrm{G}_2)\,W_{21}\right], \tag{13}$$

in which $\mathrm{sym}\,G = \frac{1}{2}(G+G^{*})$, and the G and W matrices relate surface currents to surface-tangential fields. It has been mentioned that, both the FSC and the scattering matrix method can result in compact trace formulas in terms of various matrices to compute NFRHT for any arbitrary 3D geometries. However, for the scattering matrix method, it is based on the EM fields and requires all objects to be properly arranged so that each object has to be separated by some high-symmetry shapes due to the partial-wave expansion approach. For the FSC approach, it is concerned with electric and magnetic surface currents without considering spectral bases, so it is not limited to how the objects are arranged. Furthermore, the scattering matrix method can deal with optically anisotropic properties for 2D geometries, while the FSC requires the infinite assumption (e.g. a finite dimension is approximately regarded as infinity [103]) for 2D cases and is not suitable for optical anisotropy due to the boundary element method. When considering a large number of objects, the computational costs of FSC dramatically increase due to the low solving speed of dense matrices. Up to now, the vast majority of reports in terms of the FSC approach aim to analyze NFRHT in two-body systems in a range of configurations with various shapes and finite sizes. Until very recently, the FSC approach is used to compute the NFRHT in a three-body system [73]. As its extension, the fluctuating volume-current (FVC) approach, established on the basis of the volume-integral equation (VIE) method, has been developed to deal with EM scattering in many-body systems by using volumetric currents throughout the objects [105]. The number of unknowns in FVC is much larger than in FSC formulations, but the associated VIE matrices allow for low-rank

approximations that can significantly reduce the complexity of implements thus admit practically tractable calculations.

2.1.5. Finite difference time domain method. The finite difference time domain (FDTD) method, usually used to solve the Maxwell equations by discretizing space and time to obtain the broadband frequency response of a system, can also be employed to compute heat transfer by incorporating approach incorporating the Langevin approach to Brownian motion [106, 107]. Although there have not been published works using the FDTD method to compute NFRHT in many-body systems to our knowledge, we still briefly introduce it here due to its great ability and potential. Based on the Langevin approach, the harmonic polarization response **P** of a system to the local electric field **E** are used to model the dispersive and absorbing materials, and the random source term **K**(t) is added to represent the thermal fluctuations. Then, the EM response of the system can be expressed as the following Langevin-type equation [108]

$$\frac{\mathrm{d}^2\mathbf{P}}{\mathrm{d}t^2}+\gamma\frac{\mathrm{d}\mathbf{P}}{\mathrm{d}t}+\omega_0^2\mathbf{P}=\sigma_e\mathbf{E}+\mathbf{K}(t), \tag{14}$$

where γ is a frictional coefficient denoting the losses in the system, ω_0 and σ_e represent the resonance frequency and strength, respectively. The key to this method is the implementation of the source term **K**(t), which can be enabled by combining with the FDT to obtain the frequency domain correlation $\left\langle K_\beta(\mathbf{r},\omega)K^*_{\beta'}(\mathbf{r}',\omega)\right\rangle$. For FDTD simulations, the Fourier transform allows us to get the time-domain correlation function of **K** here. Once **K**(t) is specified, equation (14) can be integrated over time to compute the fluctuating thermal radiation. The FDTD method with well-designed boundary conditions is in principle able to deal with NFRHT for arbitrary geometries and materials, but may suffer from large computational costs when the system is complicated involving 2D materials, anisotropic materials and so on.

2.2. Kinetic theory

The KT, also known as the kinetic Boltzmann approach, usually aims to predict RHT in linear chains composed of nanoparticles supporting surface resonant modes (eigenstates) [109]. In the KT approach, the energy is thought to be carried by delocalized resonant modes which propagate along the chain with a group velocity and the propagation length, determined from the complex dispersion relations of the system. Each particle behaves as a resonant cavity with strong absorption and scattering at its resonant frequency. Once the complex dispersion relation for the propagating modes is obtained, the heat flux within the system, resulting from first-order comments related to the distribution function of thermal photons obtained by the BTE, can be expressed as [110]

$$\varphi=\frac{1}{2\pi}\sum_m\int_0^\infty\hbar\omega_m(k)\,v_{g,m}(k)\,f_\mathrm{B}[\omega_m(k)]\,\mathrm{d}k, \tag{15}$$

where k is the wavevector, $\omega_m(k)$ stands for the dispersion relation of mode m, $v_{g,m}=\mathrm{d}\omega_m/\mathrm{d}k$ is the group velocity, and $f_\mathrm{B}(\omega)$ is the Bose–Einstein distribution function of plasmons (bosons) at a given temperature. However, the KT approach still has several limitations. Although it can in principle be used to describe any set of dipoles, how the KT approach can be applied to two- or three-dimensional systems of particles still remains unclear. Some previously published studies have attempted for higher-dimensional particle systems by using a higher-dimensional density of states equation, but the results have not been validated by other exact methods [111–113]. With respect to noble metals with resonance at high frequencies, the resonant modes are relatively unpopulated, so the KT approach fails to predict the heat flux and a method such as FE is required to account for RHT at lower frequencies. Another drawback of KT is that it is not adaptable for magnetic resonance and non-resonant hyperbolic modes which are frequently used to enhance NFRHT [110]. Furthermore, it has been believed that the KT approach cannot accurately describe NFRHT in both the ballistic and diffusive regimes with the chain length being much smaller and larger than the propagation length of the localized resonances along the chain, respectively [114].

3. Emerging functionalities in many-body systems

Given that there exist many challenges for precisely constructing a near-field many-body system and measuring the radiative heat flux within it, researchers mainly focus on the theoretical works by developing the above computational methods and proposing many-body heat transport phenomena. Compared to a two-body system, a many-body system with at least three objects participating in the RHT process, has been theoretically predicted to exhibit distinct transport mechanisms due to the inborn mutual interactions, leading to several emerging functionalities, including the enhancement of RHT, MO-induced heat transport, superdiffusive and ballistic heat transport, photon drag effect and collective thermal emission.

3.1. Enhanced heat transfer

NFRHT is mainly limited by the ETC for each photon tunneling channel and the total number of channels for any system. With respect to a two-body system composed of two dipolar particles, there exist only three channels (while gravitational waves cooling a star have five channels [115]) contributing to RHT due to the coupling of the three components of dipole moments, which sets the limit of the radiative thermal conductance as three times the quantum limits on rates of heat flow $\pi k_\mathrm{B}^2T/3\hbar$. However, when introducing other dipoles between them, the many-body mutual interaction can enhance the heat transfer between the two terminal dipoles (though still far away from the theoretical limit) in such a many-body system compared to the two-body system. For instance, in a discrete system consisting of three SiC (polar materials, also for SiO_2) nanoparticles which are regarded as radiating electric dipoles due to their sufficiently small sizes, Ben-Abdallah *et al* [86] investigated the RHT between two terminal particles normalized to a two-body system in the absence of the middle one by equation (9), as shown in figure 1(a). The 10-fold enhancement of thermal power exchanged in the three-body system relative to that in the two-body system can be obtained when the ratio

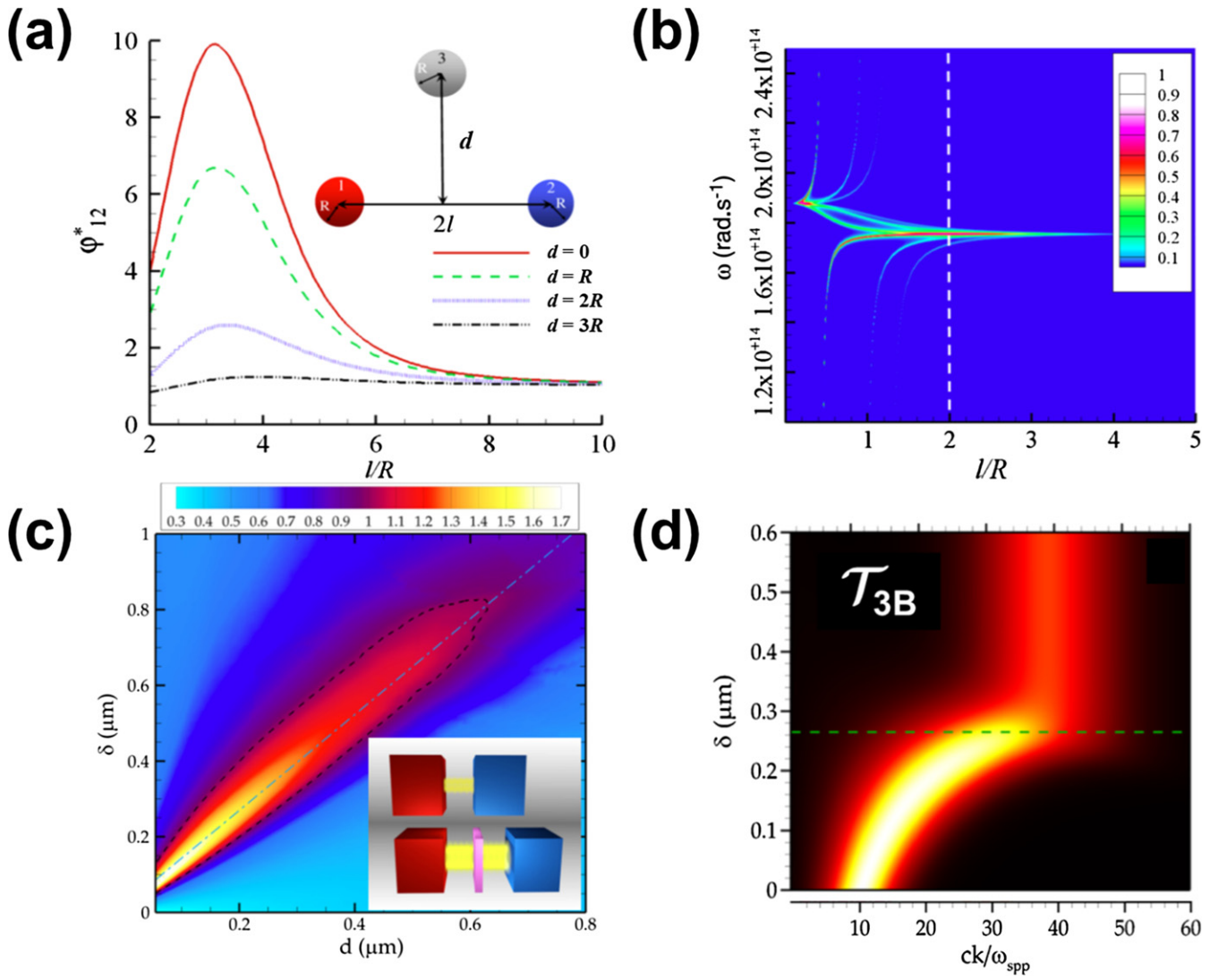

Figure 1. Enhancement of NFRHT due to many-body effects. (a) Heat fluxes between two SiC spherical nanoparticles in a three-body system (see the inset, $R = 100$ nm, $T_1 = 300$ K, $T_2 = T_3 = 0$ K) as a function of the position of the third one normalized to that without the third one. (b) ETC between two spherical SiC particles separated by a center-to-center distance $2l$ when the third SiC particle is located at the middle of this couple. (c) Total heat-flux amplification $\varphi_{3B}/\varphi_{2B}$ with respect to distance d and slab thickness δ. The inset shows the corresponding two-plate (a SiC–SiC system) configuration and the three-plate (a SiC-Drude-SiC system) configuration. The black dashed line denotes $\varphi_{3B}/\varphi_{2B} = 1$. The light blue dot-dashed line illustrates the dependence of the optimal value of δ on d. (d) ETC $\mathcal{T}_{3B}$ for ω_{spp} and $d = 200$ nm versus dimensionless wavevector ck/ω_{spp} and thickness of the intermediate plate δ. (a), (b) Reprinted figure with permission from [86], Copyright (2011) by the American Physical Society. (c), (d) Reprinted figure with permission from [72], Copyright (2012) by the American Physical Society.

of the center-to-center distance between two terminal particles and the particle radius (l/R) is around 3. This phenomenon can be explained by the distribution of ETC between two terminal particles $\mathcal{T}_{12}$ (see figure 1(b)). For the systems of two or three particles, there exist two kinds of resonances: (i) intrinsic surface resonance depending only on properties of materials, and (ii) configurational resonance which are geometric in nature due to multiple interactions of dipoles [116]. Adding a particle between two particles has no impact on intrinsic surface resonance (with $\varepsilon_{sr} = -2$ at around 1.76×10^{14} rad s^{-1}), but can modify the configurational resonances especially for small distances. For large distances, the intrinsic resonance becomes dominant, and the coupling of surface resonances between the two terminal particles becomes more efficient in presence of the middle one than the absence. This enhancement mechanism can be straightforwardly extended to a system consisting of more particles. For example, particles in reality usually get close to each other, and can even form a dense particulate many-body system (e.g. a cluster) where the fractal dimension represents the morphology of internal structure and also remarkably affects the optical responses. In this scenario, when surface resonances are supported and the nanoparticles are in the near-field, the effect of many-body interaction on NFRHT in and between fractal structures becomes important, which is closely related to arrangements, sizes, and composition of fractal structures [117–119].

In contrast to dielectric nanoparticles where only the electric dipoles are considered, the magnetic moments come into

play for metallic particles due to the existence of the eddy current, which increase the number of photon tunneling channels which is beneficial for enhancing NFRHT [120, 121]. Furthermore, the introduction of magnetic dipoles results in the coupling of electric and magnetic dipoles which can provide more extra contributions to heat transfer when many-body systems consist of both electric and magnetic dipoles. In this case, each of the four coupling terms (i.e. the electric-electric, electric-magnetic, magnetic-electric, and magnetic-magnetic terms) may dominate the RHT for some certain configurations [91, 120]. In addition, the contribution of electric and magnetic multipoles is nonnegligible at extremely short distances [90].

When the dipolar nanoparticles are optically anisotropic, RHT becomes much different from systems composed of isotropic nanoparticles having isotropic polarizability tensors as mentioned above. For example, for a small ellipsoidal nanoparticle, its polarizability tensor is diagonal in the principal-axis system, but the diagonal components are different due to the depolarization situation related to the geometry, leading to the anisotropy of particles in different orientations. In this case, the heat transfer can be enhanced by several orders of magnitude than that for isotropic particles in certain configurations, and also possess high tunability by changing their relative orientations [87].

For many-body planar systems, the vacuum cavities and interfaces form the photon tunneling channels for heat transport. Compared to the RHT between two resonant plates, a three-body planar system has more cavities and interfaces, resulting in two-fold effects: (i) the intermediate plate adds more supplementary modes due to three-body effects, leading to the enhancement and broadening of the resonance peak, which is beneficial for a higher radiative heat flux; (ii) the optical property of the tunneling medium between the two terminal plates are modified by the intermediated plate compared to a two-body system where the tunneling medium is vacuum. These effects can to some extent alleviate the intrinsic exponential damping in vacuum, and allow for huge amplification of photon heat tunneling [72]. Figure 1(c) illustrates the amplification of the total heat fluxes $\varphi_{3B}/\varphi_{2B}$, i.e. the ratio of heat flux in the three-body system to that without the middle plate. It can be seen that, even without introducing any supplementary thermal source, $\varphi_{3B}/\varphi_{2B} > 1$ in certain configurations, and the maximum $\varphi_{3B}/\varphi_{2B}$ occurs when the thickness of the middle pate δ approximately equals the interplate gap distance d. The ETC in the three-body system $\mathcal{T}_{3B}$ (see figure 1(d)), shows shift of the cutoff wavevector toward larger values when $\delta \leqslant d$, which contribute more to NFRTH but maintains a lower value in the corresponding two-body system. Replacing the intermediate plate by grating supporting hyperbolic surface modes to provide an additional photon tunneling channel [82], or by using anisotropic magneto-dielectric hyperbolic structures to support photon tunneling modes for TM and TE polarizations [81], can also lead to the enhanced RHT. In addition, if the two terminal plates are covered with monolayer graphene, changing their Fermi levels can alter the heat flux within the system. Therefore, the equilibrium temperature of the intermedia plate can be maintained in a temperature range rather than a fixed value [83].

3.2. Magneto-optical-induced heat transfer

Magnetic field can not only change the symmetry in the transport equations at the macroscale, but also act on the free electrons by Lorentz force, leading to a transversal phonon-mediated heat current at the micro/nanoscale [122, 123]. For photon-mediated heat transfer associated with optical properties of media, magnetic field can also play a role by changing the optical responses of MO materials due to the Lorentz force. In the Cartesian coordinate system, when a magnetic field along with the z axis is perpendicular to an MO material, its permittivity tensor adopts the following form [124]

$$\hat{\varepsilon}^0 = \begin{pmatrix} \varepsilon_1 & -i\varepsilon_2 & 0 \\ i\varepsilon_2 & \varepsilon_1 & 0 \\ 0 & 0 & \varepsilon_3 \end{pmatrix}, \tag{16}$$

where $\varepsilon_1(H)$ and $\varepsilon_2(H)$ are both magnetic field-dependent, due to the cyclotron frequency $\omega_c = eH/m^*$ in their expression terms with m^* being the effective mass. This permittivity tensor closely depends on the field orientation. For example, when the magnetic field with forming a polar angle θ with the z axis and lying on the x-z plane is applied, the permittivity tensor can be obtained by $\hat{\varepsilon} = R_y(\theta)\hat{\varepsilon}^0 R_y^{\mathrm{T}}(\theta)$, with $R_y(\theta) = \begin{pmatrix} \cos(\theta) & 0 & -\sin(\theta) \\ 0 & 1 & 0 \\ \sin(\theta) & 0 & \cos(\theta) \end{pmatrix}$ being the rotation matrix, as reported in [125, 126]. The appearance of the nonzero off-diagonal elements with opposite signs originates from the Lorentz force parallel to the surface induced by the external magnetic field. This introduces the asymmetry of the MO material since $\hat{\varepsilon} \neq \hat{\varepsilon}^{\mathrm{T}}$, and may break the time-reversal symmetry with the presence of nonreciprocity. Many kinds of semiconductors, including n-InSb, InAs, HgTe, GaAs, etc, have low effective masses, and hence large ω_c for a given H, leading to distinct MO responses in the mid-infrared [93, 127]. For a dipolar particle, an anisotropic permittivity tensor will directly result in an anisotropic polarizability tensor. In MO many-body particulate systems, the external magnetic field enables the active control of the magnitude and direction of radiative heat flux, and also allows for nonreciprocal RHT with unprecedented heat transport mechanisms.

3.2.1. Thermal Hall effect. If electric current flows through a conductor or semiconductor in a magnetic field, the moving charge carriers experience the Lorentz force induced by the perpendicular component of the magnetic field, allowing for the generation of an asymmetric distribution of charge density. This phenomenon is called the Hall effect that was discovered by Edwin Hall in 1879 [128]. The thermal analog of this classical Hall effect has been predicted in photon-mediated RHT, i.e. the magnetic field enables the existence of the radiative heat flux in the direction perpendicular to the initial temperature gradient [76]. As shown in figure 2(a), there are four MO nanoparticles participating in NFRHT, constituting a many-body system with a discrete C_4 symmetry. In the absence of an external magnetic field, all four particles are optically isotropic so that the system is thermally symmetric. The two particles in

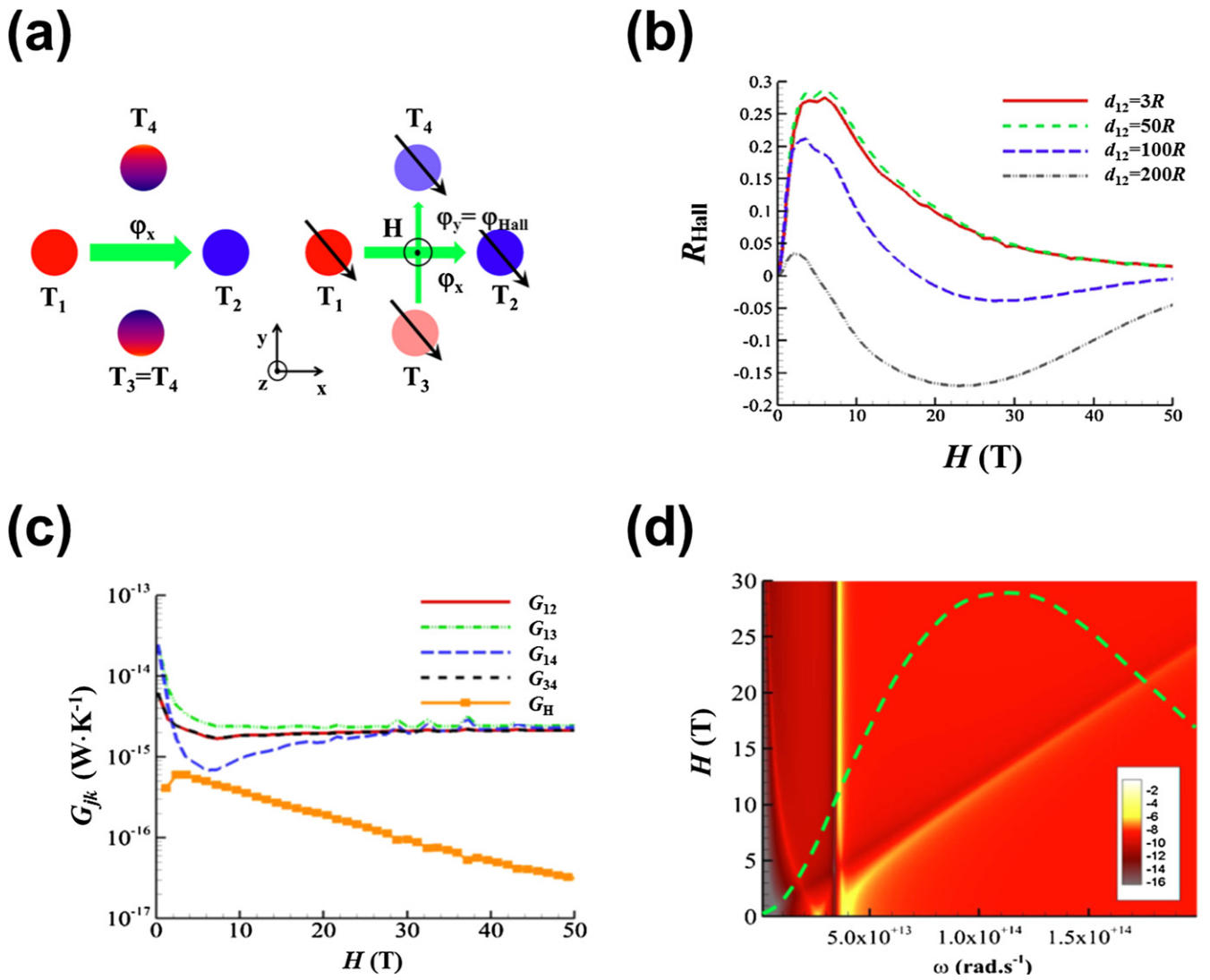

Figure 2. Photon thermal Hall effect. (a) Sketch of a four-particle configuration made with MO material used to explain the photon thermal Hall effect. The left and right two particles are held at two different temperatures T_1 and T_2. When $H = 0$, the system is thermally symmetric with all particles being optically isotropic, and there exists no heat flux in the y direction with $\varphi_y = 0$ due to $T_3 = T_4$. When a z-direction magnetic field is applied, the system symmetry is broken because all particles become optically anisotropic, and a longitudinal nonzero heat flux in the y direction $\varphi_y \neq 0$ (i.e. the Hall flux $\varphi_{\rm Hall}$) appears due to temperature gradient with $T_3 \neq T_4$. (b) Relative Hall temperature difference $R_{\rm Hall}$ for different separation distances versus the magnetic field intensity H. (c) Thermal exchange conductances G_{12}, G_{13}, G_{14}, G_{34}, and Hall conductance $G_{\rm H}$ at $T_{\rm eq} = 300$ K with respect to the magnetic field intensity H when $d_{12} = d_{34} = 3R$. (d) Resonance conditions of InSb particles in vacuum for different H. The dashed line denotes the Planck function with arbitrary unit at 300 K. Reprinted figure with permission from [76], Copyright (2016) by the American Physical Society.

the x direction have a temperature difference $\Delta T = T_1 - T_2$ so that a transverse heat flux between them exists. Meanwhile, the other two unthermostated particles at an identical temperature ($T_3 = T_4$) due to the symmetry reasons have a null radiative heat flux. However, when an external magnetic field is applied to the system orthogonally (z direction), it makes the particles biaxial and breaks the symmetry of the system. A temperature gradient of $T_3 \neq T_4$ is generated in the y direction, leading to the occurrence of a nonnull longitudinal heat flux φ_y, termed as a photon-mediated thermal Hall flux $\varphi_{\rm Hall}$. The thermal Hall flux cannot exist in two-body systems due to the second law of thermodynamics.

The relative Hall temperature difference $R_{\rm Hall} = \frac{T_3 - T_4}{T_1 - T_2}$ is used to evaluate the magnitude of the photon thermal Hall effect. Figure 2(b) shows $R_{\rm Hall}$ as a function of the magnitude intensity H when the InSb particles are embedded in a vacuum ($\varepsilon_h = 1$). In the absence of magnetic field, $R_{\rm Hall}$ equals zero for any separation distance, while shows a nonzero value when a magnetic field is applied. The thermal conductances between different particles, i.e. $G_{jk} = \frac{\partial \varphi_{jk}}{\partial T}\Big|_{T=T_{\rm eq}}$, with respect to H are depicted in figure 2(c). It can be seen that, G_{13} always exceeds G_{14}, leading to that particle 3 becomes hotter than particle 4 in figure 2(a), and thus $\varphi_{\rm Hall}$ is generated between them. This phenomenon can be explained by the resonance of the InSb particle in vacuum for different H (see figure 2(d)). The vertical branch corresponding to the excitation of surface phonon polaritons (SPhPs) of InSb particle is independent on the magnetic field, but the other branches

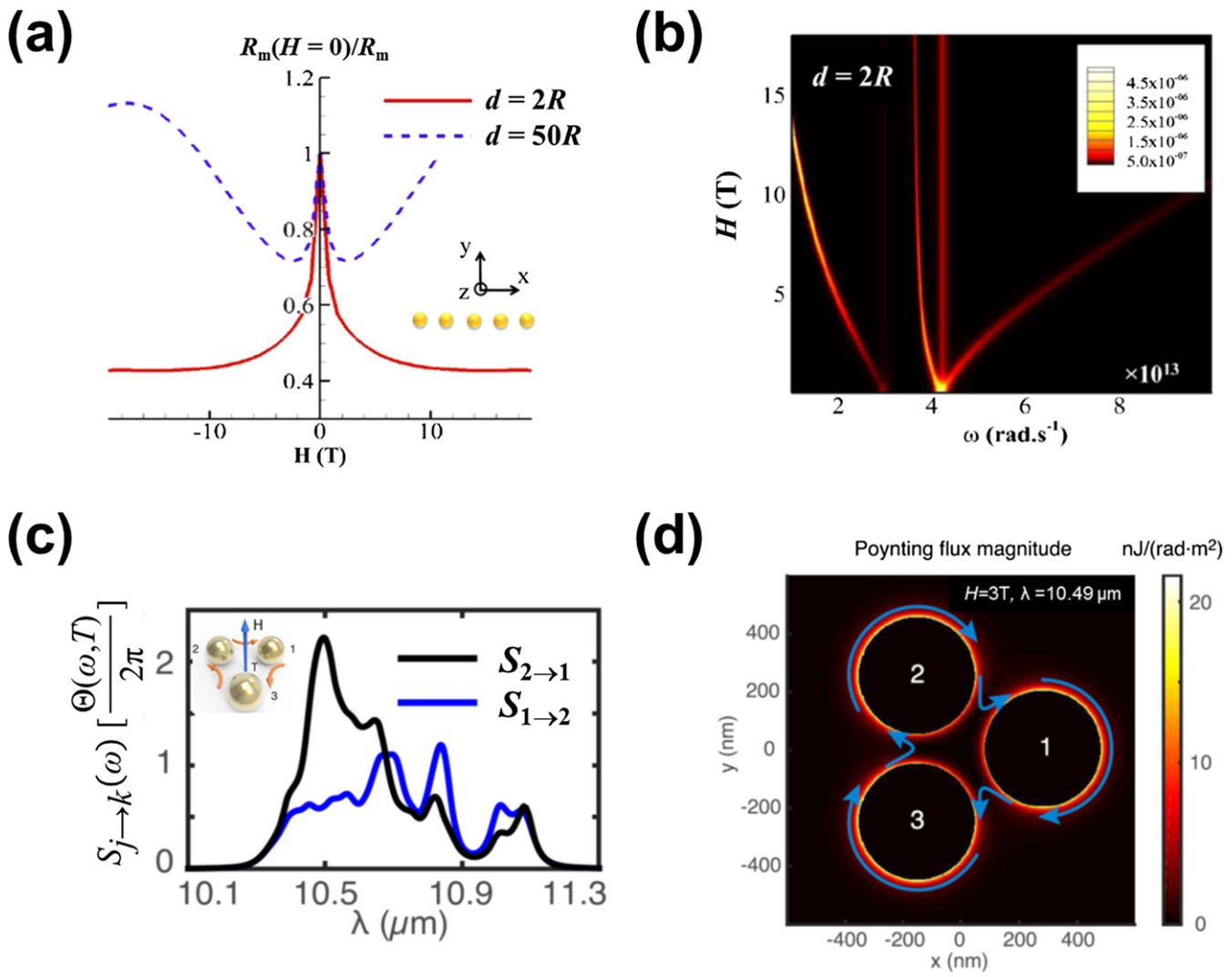

Figure 3. GTMR and persistent directional heat current. (a) Thermal magnetoresistance R_m of linear InSb nanoparticle chains versus the external magnetic field H at 300 K, for interparticle separation distances $d = 2R$ (in the near field) and $d = 50R$ (in the far field). (b) ETC $\mathcal{T}_{1N}$ in the (ω, H) panel for a linear chain of $N = 5$ InSb particles of radius of $R = 100$ nm. The edge-to-edge interparticle separation distance is $d = 2R$. (c) Heat transfer spectra of $S_{2\to1}$ and $S_{1\to2}$ at equilibrium state, in a many-body system consisting of three MO spheres with C_3 symmetry when a magnetic field is applied. (d) Poynting flux magnitude at 300 K, $\lambda = 10.49$ μm, and $H = 3$ T. The arrows denote the energy streamlines. (a), (b) Reprinted figure with permission from [74], Copyright (2017) by the American Physical Society. (c), (d) Reprinted figure with permission from [75], Copyright (2016) by the American Physical Society.

due to the plasmonic nature induced by the magnetic field, i.e. magnetization-induced plasmonics, is very sensitive to H. This unprecedented prediction has the potential to be applied in magnetic field detection in a purely thermal manner and direction modulation of heat flow, and also inspires researchers to investigate the effects of magnetization-induced plasmonics on NFRHT in many-body systems.

3.2.2. Giant thermal magnetoresistance. The giant magnetoresistance (GMR) is the magnetic field-induced large change (in general a reduction) in the electrical resistance observed in multilayers composed of alternating ferromagnetic and non-magnetic conductive layers. The GMR effect originates from the dependence of the electrical conduction in ferromagnetic materials on the spin state of the electrons. For heat transfer governed by thermal photons, there also exist the GMR effect, termed giant thermal magnetoresistance (GTMR), in MO many-body systems out of thermal equilibrium [74]. For clarity, the thermal magnetoresistance of the chain with N particles R_m is defined as the inverse of thermal conductance, i.e. $R_m = \frac{1}{G_{1N}}$. Then, the ratio $R_m(H=0)/R_m$ can be calculated to evaluate the influence of the magnetic field on RHT. Considering a linear InSb nanoparticle ($R =$ 100 nm) chain with $N = 5$ immersed in an external magnetic field of strength H orthogonal to the chain axis, R_m can be significantly increased with a magnetic field perpendicular to the chain axis (see figure 3(a)), demonstrating the existence of the GTMR. It can also be predicted that, the resistance increment can reach about 70% when $H = 2$ T, and is larger for more intense fields. As H increases, R_m increases in dilute chains ($d = 50R$) before reaching a plateau, while decreases in dense chains ($d = 2R$). Figure 3(b) shows the ETC $\mathcal{T}_{1N}$ when $d = 2R$ with $N = 5$, it can be seen that there exist two branches

associated with localized resonances exhibiting a remarkable dependence on H. Therefore, the GTMR originates from the strong spectral shift of magnetization-induced plasmonics supported by the particles, which also appears in two-body MO systems [125]. According to the linear response of heat flux to the temperature difference, the GTMR can be exploited to make a direct evaluation of the heat flux propagating in the network and even the nonreciprocity degree of a MO many-body system.

3.2.3. Persistent directional heat current. The second law of thermodynamics tells us that, for a system subject to the constraint of Lorentz reciprocity, the net heat flow between them must be 0 in thermal equilibrium, because the heat current only occurs in the presence of temperature difference. However, when the Lorentz reciprocity is broken, heat current may occur in a thermal equilibrium state without violating the second law of thermodynamics. Zhu *et al* [75] investigate the effects of the external magnetic field on NFRHT in a three-body system consisting of InSb nanoparticles forming an equilateral triangle with discrete C_3 symmetry (see figure 3(c)). In such a system with rotational symmetry, each body j supports a counterclockwise-rotating mode $|j\uparrow\rangle$ and a clockwise-rotating mode $|j\downarrow\rangle$, and these two modes are assumed that they have the identical internal decay rate. When no magnetic field is applied, the system remains reciprocal state and these two modes have the same resonant frequency ω_0. Hence, there exists no heat current when all particles have the same temperature in this case. When a magnetic field is applied perpendicular to the particle plane, the Lorentz reciprocity of the system is broken. The magnetic field splits the frequencies of the two modes into ω_{0+} and ω_{0-}, respectively, and lifts the degeneracy between the two states, resulting in that the system shows persistent directional heat current even in thermal equilibrium state. By analyzing the heat flux $S_{j\to k}$ received by body k from body j, $S_{1\to 2} \neq S_{2\to 1}$ is found in thermal equilibrium in a three-body system, demonstrating the existence of a persistent heat current which is manifested by the Poynting flux identified by the energy streamlines in the same direction (see figure 3(d)). The presence of the persistent heat current does not violate the second law of thermodynamics because the total net heat flux into each body is still 0. For a two-body system, the net heat flux between them in thermal equilibrium must be 0, which is independent of whether the system is reciprocal or not. Physically, this is attributed to that $S_{1\to 2} = S_{2\to 1}$ at all frequencies even in the presence of the magnetic field.

In essence, the above fascinating phenomena induced by MO effects can be understood by the magnetic-field-dependent circular heat fluxes, i.e. the azimuthal component of the Poynting vector around dipolar MO particles, which results from the presence of nonzero off-diagonal elements of the polarization tensor under magnetic field. In this case, the dipolar resonances split in frequency, leading to the different contribution of the resonances to the heat flux for different magnetic quantum numbers. In addition, the circular heat fluxes show strong dependence on the magnetic-field intensity and the configuration (i.e. various directions of the circularity in different symmetric configurations) [129].

3.3. Superdiffusive and ballistic heat transport

In general, heat spatially spreads from high-temperature regions to low-temperature regions in a system, leading to the formation of temperature distribution $T(\mathbf{r}, t)$ which evolves as a generalized random walk with a probability distribution function $p(x)$ of step length ($x = |\mathbf{r} - \mathbf{r}'|$). $p(x)$ is strongly related to the transport speed of heat carriers and to the distance between two successive collision events. In solid, the heat carriers (phonons or electrons) randomly move through the atomic lattice with a Gaussian $p(x)$ so that all its moments $\int x^n p(x)\,\mathrm{d}x$ are finite and the transport regime of heat conduction is a normal diffusion process. However, if $p(x)$ decays algebraically and shows a non-integrable behavior, at least one of its moments will be divergent and the heat transport regime becomes superdiffusive [130]. In a 1D ordered particulate many-body system, i.e. a particle chain as shown in figure 4(a), the thermal conductance shows an asymptotic behavior for large separation distance Δx. For a dense chain with $d = 3R$ (in the near field), the intense near-field collective effects enable its diffusion coefficient for long distances to be diverging, more concretely, scale with $(\Delta x)^{-2}$, demonstrating the superdiffusive behavior of heat transport. This nonlocal behavior allows to go beyond the normal diffusion limit in solids, and design materials with faster heat transport mechanism for thermal management. When in a diluted chain with $d = 50R$ (in the far field), all particles exchange heat in an independent manner, so that the thermal conductance follows a $(\Delta x)^{-2}$ power law. The similar diffusive regimes also exist in 3D disordered networks.

For a planar many-body system composed of polar materials, the steady-state temperature profile $T(x, t)$ also illustrates different diffusive regimes [131]. Assuming that thermal radiation is the only source of heat relaxation, the steady-state temperature profile with respect to the position is shown in figure 4(b). In a dilute system with the interplate distance $d = 500$ nm, the resultant short-range couplings cause the heat transfer to decay exponentially so that the temperature profile decreases smoothly, demonstrating that the regime of heat transport is superdiffusive. In a dense system with $d = 5$ nm, the regime of heat transport undergoes the diffusive-to-ballistic transition indicated by the change of the heat transfer coefficients from an exponential decay to a power-law decay. This is because that the polarization of dominant modes changes from TM to TE according to the polarization contributions to the heat transfer coefficients, see details in [131]. Furthermore, for a many-body system consisting of graphene, the heat transport regime, showing strong dependence on chemical potentials of graphene due to the characteristics of graphene SPPs, suffers a monotonic transition from diffusive to quasi-ballistic transport [132].

3.4. Thermal photon drag effect

For electrons, their interactions lead to the coupling of a pair of electric conductors when the separation distance is within the range of Coulombic interactions. Therefore, when an electric current flows in the (drive) conductor, it will induce a

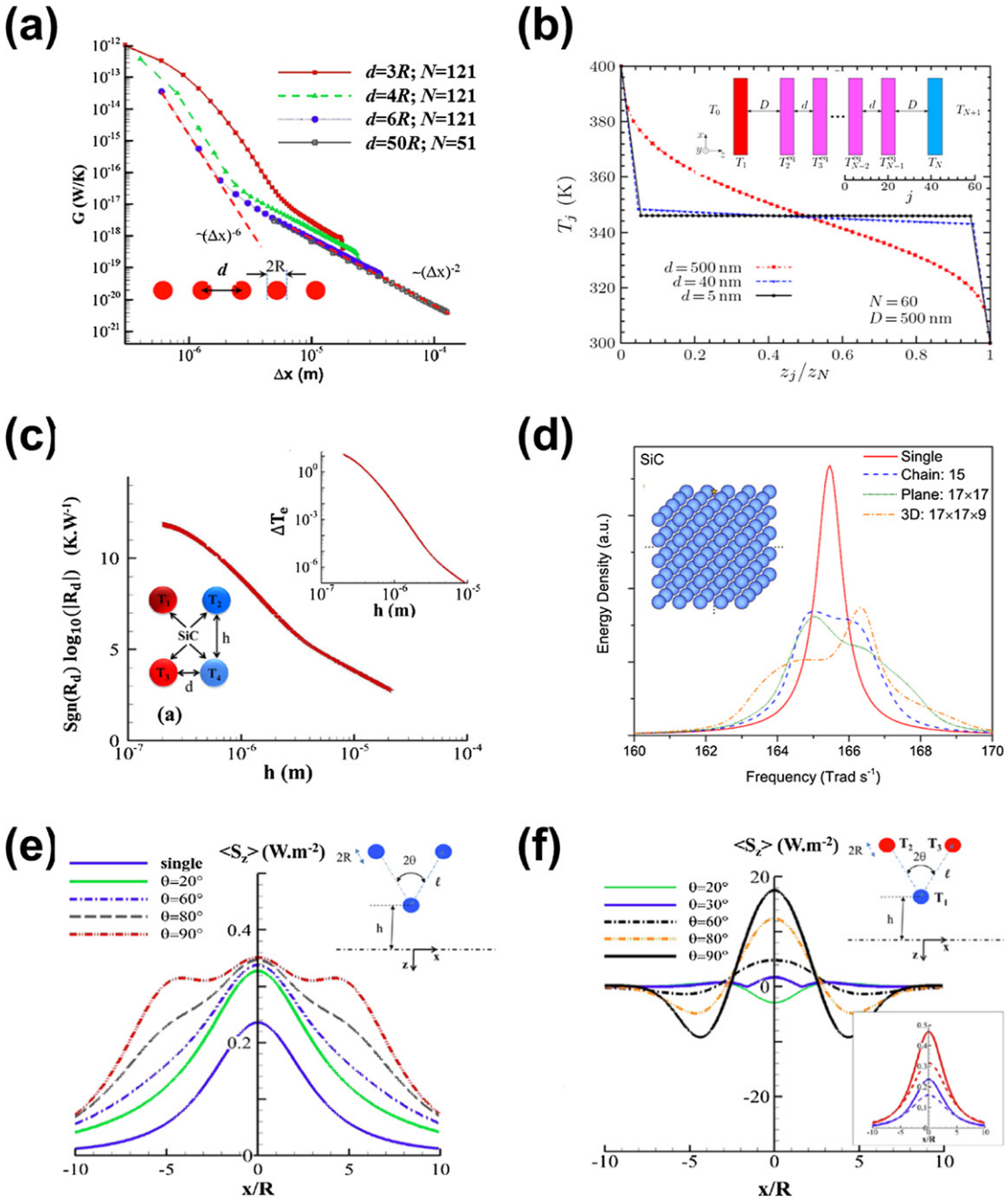

Figure 4. (a) Thermal conductances for a chain of SiC nanoparticles (see the inset) with different configurations as a function of the separation distance. (b) Schematic (see the inset) of an N-body system comprising N-2 SiC plates interacting two external SiC plates at fixed temperatures T_1 and T_N, and the steady-state temperature profile as a function of the normalized position z_j/z_N. (c) Drag resistance between two dimers of SiC nanoparticles with radii of 100 nm under a primary temperature difference $T = T_1 - T_2 = 50$ K when $T_2 = 300$ K with respect to the dimers separation distance h. (d) Spectral energy density of emitted near-field thermal radiation from SiC nanoparticles in different arrays including single particle, chains, planes, and 3D arrays (see the inset). (e) Normal component $\langle S_z \rangle$ of the Poynting vector radiated through the surface $z = 0$ by a three-tip configuration made with SiO_2 nanospheres held at the same temperature for different angular openings ($T = 300$ K, $R = 20$ nm, $h = 4R$, and $l = 5R$). The blue solid line corresponds to the case of a single nanoemitter located at $z = -h$. (f) Normal component $\langle S_z \rangle$ of the Poynting vector radiated through the surface $z = 0$ by a three-tip configuration made with SiO_2 nanospheres held at $T_1 = 300$ K and $T_2 = T_3 = 350$ K (red) for different angular openings ($R = 20$ nm, $h = 4R$, and $l = 5R$). The inset shows the flux at $z = 0$ for a single emitter at $T = 350$ K (red) and $T = 300$ K (blue) at $z = 4R$ (solid) and $z = 4R + l\cos(80)$ (dashed). (a) Reprinted figure with permission from [130], Copyright (2013) by the American Physical Society. (b) Reprinted figure with permission from [131], Copyright (2018) by the American Physical Society. (c) Reprinted figure with permission from [134], Copyright (2019) by the American Physical Society. (d) Reprinted figure with permission from [135], Copyright (2017) by the American Physical Society. (e) Reprinted figure with permission from [136], Copyright (2019) by the American Physical Society.

current via Coulomb drag effect in the other (passive) conductor in the proximity of it [133]. Whether do the thermal photons, which is strongly relevant to electrons, result in a similar phenomenon?

Considering a many-body system composed of two parallel pairs of SiC nanoparticles (see the inset of figure 4(c)) where heat exchanges are governed by thermal photons, a temperature difference is initially held within one (drive) pair while the other pair (passive) is left free. The thermal drag resistance, defined as $R_{\mathrm{drag}} = \frac{\Delta T_{\mathrm{p}}}{\varphi_{1N}}$ with ΔT_{p} being the temperature difference of the passive pair induced by the drive heat flux φ_{1N}, is positive and monotonically decays with the separation distance between the two pairs, as shown in figure 4(c). The direction of heat flux induced in the passive pair depends on the strength and the nature of mutual interactions between the particles. Furthermore, for nonreciprocal many-body systems, the heat supercurrents supported by these systems can either be amplified or inhibited by this frictional drag effect [134].

3.5. Collective near-field thermal emission

NFRHT, mainly transported by evanescent waves, is consequently nonradiative, but it still can play a pronounced role in thermal emission to the far field, corresponding to the spectral density of emitted energy rather than the power exchanged as mentioned above [135]. In a many-body system consisting of polar nanoparticles, including chains, planes, and three-dimensional (3D) arrays (see the inset of figure 4(d)), the propagating SPPs through the collective effect have a remarkable effect in their emission spectra, and the emission characteristics are very different in the presence or absence of the propagating modes. For a SiC nanoparticle array having the long-range coupling of propagating SPhPs, the thermal emission changes significantly with the system changing from a single particle to a chain, plane, or 3D array, accompanied with the dramatic reduction of the emission peak and its splitting into multiple peaks covering a broader spectral region, as shown in figure 4(d). However, in the absence of long-range coupling, e.g. in a SiO_2 nanoparticles array, the thermal emission spectra change little as more particles are added.

Recently, Ben-Abdallah [136] theoretically investigates the thermal emission of a set of interacting nanoemitters held at certain temperatures. For concreteness, as illustrated in the inset of figure 4(e), a triangular three-tip scanning thermal microscope (SThM) platform is considered. Each tip, behaving as the single thermal emitter at temperature T_j, is positioned and thermally controlled individually. In this scenario, all emitters are thermalized at the same temperature. For different angular openings θ, the normal components $\langle S_z \rangle$ of the Poynting vectors radiated through the surface $z = 0$ at the distance of $h = 4R$ in the steady state are shown in figure 4(e). It can be observed that, the FWHM of heat flux slightly increases with θ, due to the superposition of heat flux radiated by these fluctuating dipoles and many-body cooperative effects. When the system is out of thermal equilibrium, for example, three tips in the SThM platform are thermalized at $T_1 = 300$ K and $T_2 = T_3 = 350$ K as shown in figure 4(f). When $\theta = 20^\circ$, the heat flux propagates toward the emitting system itself manifested by the negative $\langle S_z \rangle$ around $x = 0$, indicating that this multi-tip setup acts as a local heat pump. For large angular openings, this pumping effect is off center with the negative $\langle S_z \rangle$ occurring away from $x = 0$. Furthermore, compared to the results of three tips at the same temperature (see figure 4(e)) or a single emitter (see the inset of figure 4(f)), the heat flux in this case can be remarkably focused on a smaller spot with a much smaller FWHM, and can be enhanced by 2 orders of magnitude.

4. Enabling applications using many-body systems

Thermal devices mediated by radiative photons are superior to phononic thermal devices to manage the heat flux at the nanoscale in some aspects [137–139]. The radiative photons transport with the speed of four or five orders of magnitude larger than the speed of conductive heat carriers (acoustic phonons). RHT within photonic devices avoids the inevitable local Kapitza resistances within which come from the mismatch of vibrational modes at the interfaces and remarkably suppress the phononic heat flow. Moreover, the strong nonlinear phonon–phonon interactions in phononic devices make them difficult to deal with in the presence of a large thermal gradient. Therefore, an increasing number of photon-mediated devices are proposed for high-efficiency energy utilization and thermal management at the nanoscale.

4.1. Thermal waveguide

A photon-mediated thermal waveguide is used to extract the nonradiative waves, which are naturally confined on the interfaces, for long-distance heat transport. As well known, if a medium has a high dielectric permittivity ε with negligible loss, it can support propagating modes with lateral wavevectors up to $\sqrt{\varepsilon}\omega/c$ larger than ω/c in vacuum. If the medium has hyperbolic dispersion relations, it can in principle support the propagation of evanescent waves without the limit of lateral wavevectors, i.e. high-k modes. These mechanisms allow the evanescent waves with large lateral wavevectors to become propagating within the medium, which dramatically alleviate their exponential damping to realize the thermal waveguide. For example, when the middle plate in a three-body system is a hyperbolic material (HM) plate (see the inset of figure 5(a)), the evanescent waves radiated from the left plate partially become propagating inside the middle one and can travel through it to couple with the right one. If the two terminal plates support surface resonances, the high spectral heat flux peak due to the resonance can be enhanced and broadened. For concreteness, when a hypothetical plate with $\varepsilon_x = 5$ and $\varepsilon_z = -1$ (type I hyperbolic modes with a two-fold hyperboloid) is intercalated between two SiC terminal plates, the radiative heat flux exceeds the blackbody limit by around 13 times when the thickness of the intermediated plate is 100 μm, which is evidently in the far-field regime, as shown in figure 5(a) [57]. Figure 5(b) illustrates the ETC $\mathcal{T}_{12}$ for p polarization, and shows the coupling of the surface modes and the Fabry–Pérot modes in the hyperbolic plate, which provides the

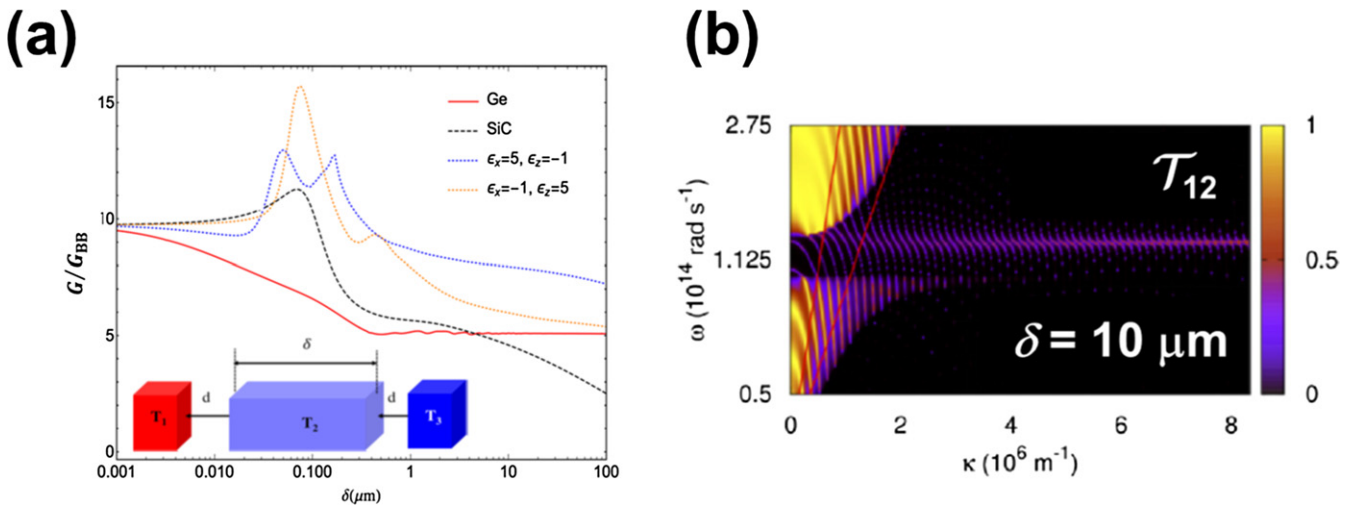

Figure 5. (a) Heat transfer coefficient ratios G/G_{BB} for a SiC–HM–SiC system (see the inset) versus the thickness δ for different intermediate slabs for a gap distance of $d = 100$ nm. (b) ETC $\mathcal{T}_{12}$ for p polarization in the SiC–HM–SiC system for p polarization for $d = 100$ nm and $\delta = 10$ μm of the intermediate hyperbolic plate with $\varepsilon_x = 5$ and $\varepsilon_z = -1$ in (ω, κ) space. The inserted lines are the light line in vacuum. Reprinted figure with permission from [57], Copyright (2016) by the American Physical Society.

coupling channels of the surface modes through the hyperbolic waveguide. For two nanoparticles, the long-distance radiative heat transport can also be realized by comprising a mixed many-body system. For example, by putting a surface-resonant substrate underneath two SiC nanoparticles in the near field, the strong coupling of the localized SPhP of SiC nanoparticles to the propagating SPhP of the substrate provides more tunneling channels, and thus remarkably enhances the RHT by orders of magnitude at large distances ($>\lambda_{\mathrm{th}}$) [140]. If the substrate is replaced by an array of graphene strips which behaves as a metasurface supporting anisotropic and tunable SPPs, RHT between two nanoparticles can even be modulated due to the strong dependence on the geometry and the chemical potential of the graphene strips [141].

4.2. Heat engine

In thermodynamics and engineering, a heat engine is a device to do mechanical work by converting thermal energy into mechanical energy. Contactless devices transfer heat by radiation and thus circumvent the intrinsic drawbacks (e.g. local Kapitza resistances and low speed of phonons) of conductive devices. In particular, the near-field thermal radiation energy conversion is more efficient, which provides high possibility for utilizing low-grade waste heat. The concept of heat engine using NFRHT in a two-body system has been proposed, which has a good performance when polar materials are used [142]. According to the passive amplification mechanism in a three-body planar system as discussed in section 3.1, a three-body heat engine driven by photon tunneling is presented to further improve the efficiency of energy conversion [84]. Considering a three-body system as illustrated in lower part of figure 6(a), the emitter at a temperature T_{h} is thermalized by the heat source and the receiver at temperature T_{c} by the heat sink, while a passive intermediate plate with thickness of δ is placed between them. For simplicity, for an N-body (NB) system, the net energy and entropy fluxes on the cold body are denoted as $\varphi_{N\mathrm{B}}$ and $\psi_{N\mathrm{B}}$. Thus, the maximum work flux and the maximum efficiency can be given by $\dot{\mathcal{W}}_{N\mathrm{B}} = \varphi_{N\mathrm{B}} - T_{\mathrm{c}}\psi_{N\mathrm{B}}$ and $\overline{\eta}_{N\mathrm{B}} = \frac{\dot{\mathcal{W}}_{N\mathrm{B}}}{\varphi_{N\mathrm{B}}}$, respectively, of which the dependencies of $\dot{\mathcal{W}}_{N\mathrm{B}}$ and $\overline{\eta}_{N\mathrm{B}}$ on T_{h} with T_{c} fixed at 300 K are shown in figure 6(b). Thanks to the photon-tunneling enhancement in the three-body system, $\dot{\mathcal{W}}_{3\mathrm{B}}$ is always larger than $\dot{\mathcal{W}}_{2\mathrm{B}}$ for any T_{h}, and the discrepancy between them grows monotonically, though $\overline{\eta}_{3\mathrm{B}}$ is slightly smaller than $\overline{\eta}_{2\mathrm{B}}$.

4.3. Heat pump

An electrical pump is a device that can transfer fluids (liquids or gases) through mechanical action which is controlled by a bias voltage. In analogy with the electrical pumping, the radiative heat-pumping effect has been theoretically predicted [143]. Considering a three-body system consisting of three SiC spherical nanoparticles as shown in figure 6(c), particles 1 and 2 in thermal equilibrium constitute the reference system, while particle 3 behaves as the external source to pump the radiative thermal power exchanged between particles 1 and 2. Particle 3 has the periodic modulation of $T_3(t) = T_{3,\mathrm{eq}} + \Delta T \sin(\omega t)$ and $x_3(t) = \Delta x \sin(\omega t + \phi)$, where $T_{3,\mathrm{eq}}$ corresponds to the temperature in thermal equilibrium when the power absorbed by particles 1 and 2 vanishes, Δx and ΔT are the displacement and temperature oscillation amplitudes, ω is the resonance frequency of SiC nanoparticle, and ϕ is the dephasing. According to the power absorbed by each particle with respect to time during one period of modulation of particle 3 (see figure 6(d)), it can be seen that the energy transfer between particles 1 and 2 at thermal equilibrium, can be produced by the presence and simultaneous variation of Δx and ΔT of particle 3 in the system. This phenomenon demonstrates the presence of radiative heat pumping effect. In this radiative heat pump, the negative differential thermal resistance within the system is unnecessary, and it also not restricted to the existence of exotic topological characteristics in non-Hermitian systems [144, 145].

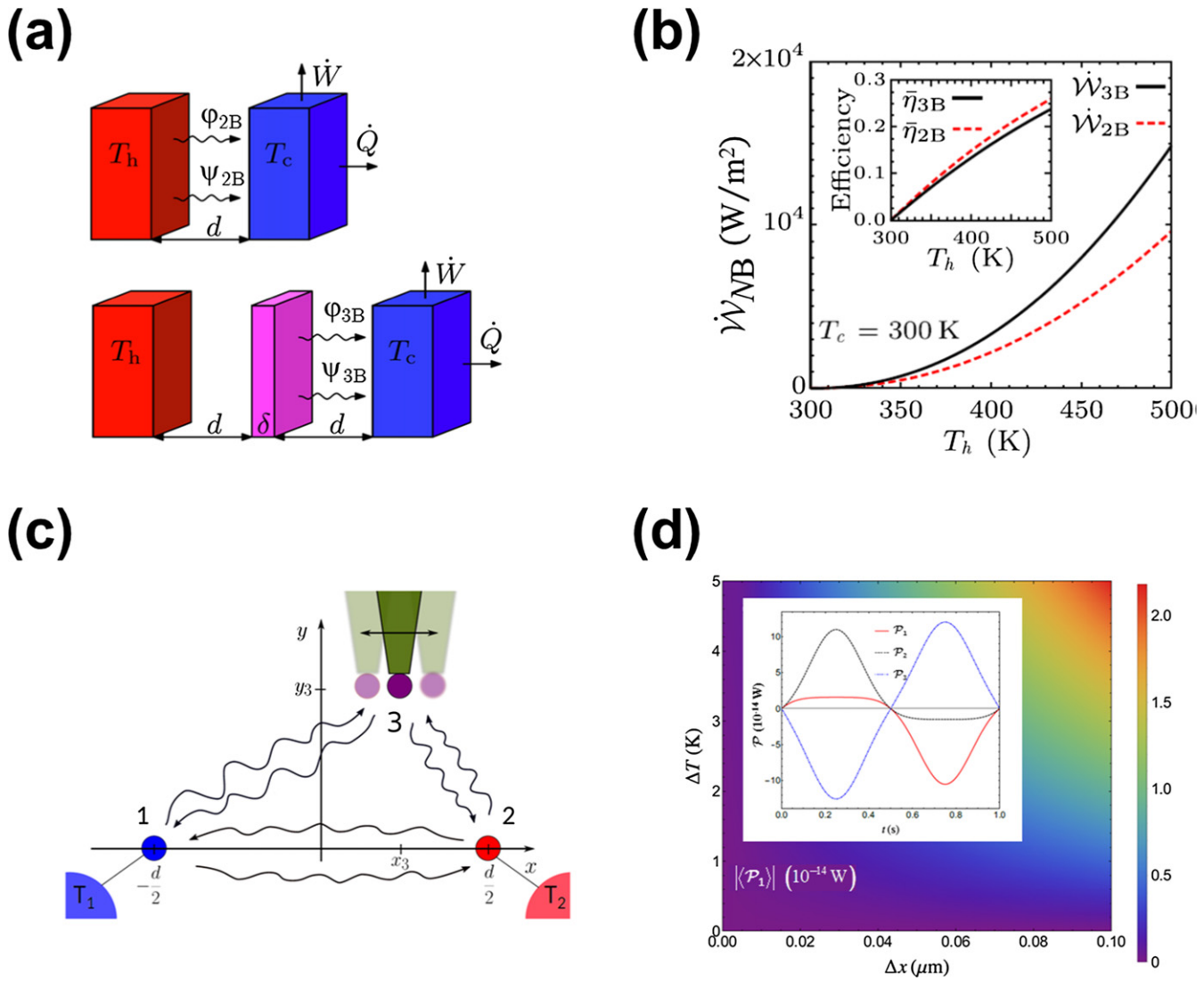

Figure 6. (a) Sketch of a three-body heat engine with a hot source at temperature T_h and a cold sink at temperature $T_c(<T_h)$. The terminal plates are respectively thermalized with the source and sink, while a passive intermediate plate (of width δ) is placed between them. The engine yields a usable work flux $\dot{W}$ by converting NFRHT, while the cold sink receives a heat flux $\dot{Q}$. (b) Maximum work fluxes for the three-body (see the inset) and two-body configurations, respectively, as a function of the temperature of the hot source T_h. (c) Geometry of a three-body system to demonstrate the radiative heat pumping effect. Particle 3 oscillates periodically along the x direction. (d) Absolute value of the average power absorbed by particle 1 over one period as a function of Δx and ΔT, respectively. The inset shows the powers absorbed by particles 1 (solid red line), 2 (dashed black line) and 3 (blue dot-dashed line) as a function of time for the periodic variation. (a), (b) Reprinted figure with permission from [84], Copyright (2015) by the American Physical Society. (c), (d) Reprinted figure with permission from [143], Copyright (2020) by the American Physical Society.

4.4. Heat flux switch and splitter

Active control of NFRHT is a hot topic due to the great potential to manage heat transport at the nanoscale [146–148]. Very recently, it has been experimentally demonstrated that the far-field RHT can be dramatically suppressed by putting a substrate in the near field [73]. In a three-body system, two coplanar SiN membranes separated by a fixed distance of $g = 20\ \mu$m (in the far-field regime) are the emitter and receiver, and the substrate under them with a vertical gap distance of d is the modulator, as shown in figure 7(a). Figure 7(b) shows the radiative conductances G_{e-r} as a function of d for the modulator with thicknesses of 524 nm and 3.3 μm. It can be seen that, by simply sweeping the vertical separation distance ranging from 18 to 3 μm away from the underneath substrate, G_{e-r} shows a remarkable change with a maximum measured switching ratio of 2.8 (define as $G_{e-r,max}/G_{e-r,min}$). It can be explained be the x-direction Poynting flux P_x at $\lambda = 16.5\ \mu$m in the three-body system. When the vertical gap $d = 20\ \mu$m, P_x is largely confined to the plane of the emitter and receiver (see figure 7(c)). However, when d is reduced to 3 μm, P_x effectively leaks into the modulator (guided by evanescent interactions) rather than traversing the lateral gap to the receiver (see figure 7(d)).

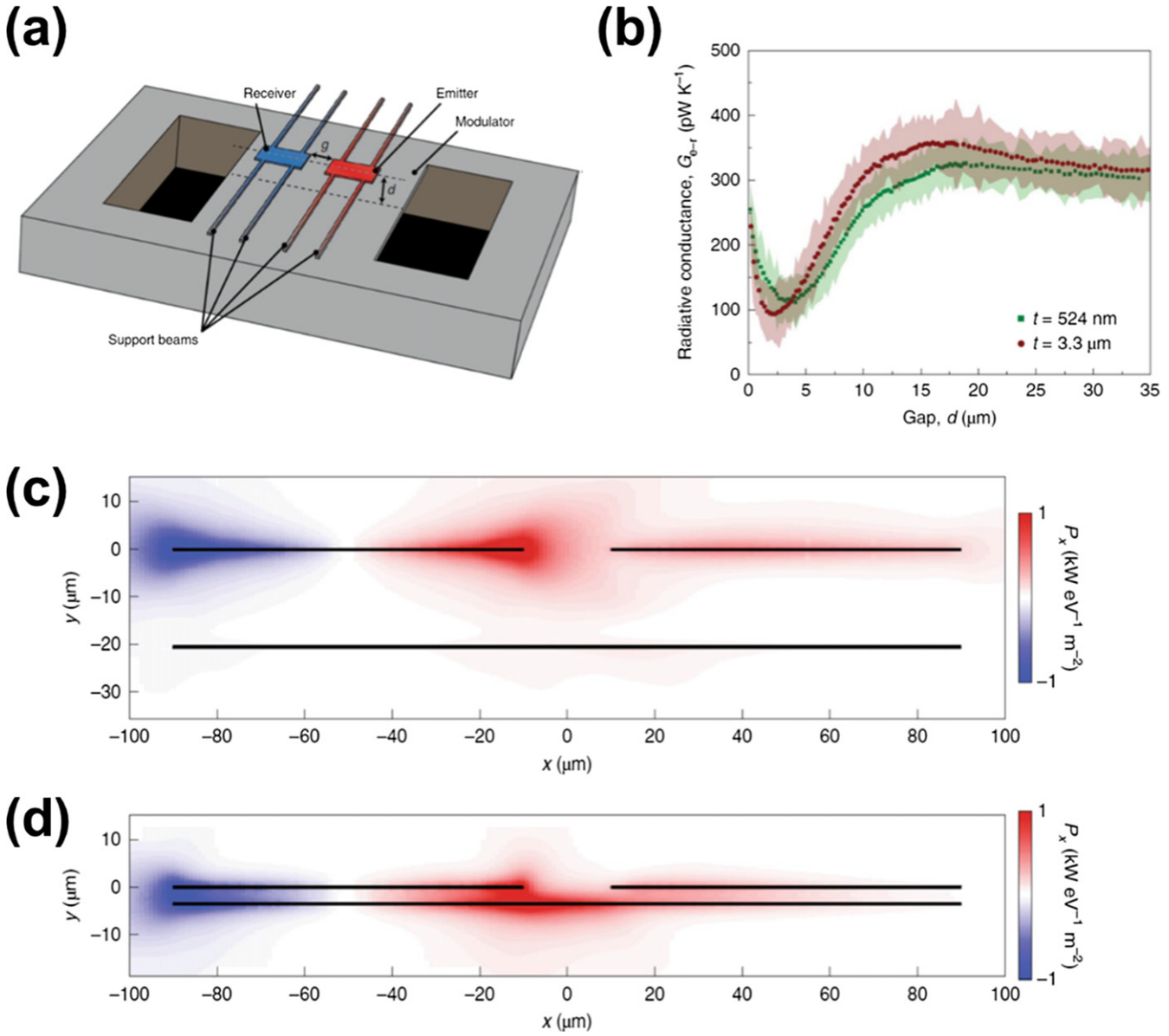

Figure 7. (a) Schematic of experimental setup of the three-body system composed of the emitter, receiver and modulator. (b) Measured radiative conductance G_{e-r} as a function of gap distance d for the 524 nm-thick (green) and 3.3 μm-thick (brown) SiN modulator. (c) Computed x-direction Poynting flux P_x at $\lambda = 16.5$ μm due to thermally induced radiation sources on the surface of the emitter (top left, held at 300 K) after a 524 nm-thick SiN slab is introduced. The vertical gap between emitter and modulator is $d = 20$ μm (in the far field). (d) Same as in (c) but for $d = 3$ μm (in the near field). Reprinted by permission from Springer Nature Customer Service Centre GmbH: Nature Nanotechnology. [73] (c) 2020.

A high thermal switching ratio can lead to directional heat flow in many-body particulate systems, allowing for the splitting effect of the radiative heat flux. Due to the excellent tunability of graphene by changing its Fermi level, it is frequently used to manage the NFRHT by adjusting its surface plasmons in the mid-infrared range [30, 61]. In a many-body system composed of graphene nanodisks which can be regarded as electric diploes due to their sufficiently small sizes [149], the NFRHT within this system can be tuned by changing their Fermi levels to alter the match state of optical properties (described by the polarization tensors) which play an important role in photon tunneling [88]. Moreover, rotating the nanodisks may break the spatial symmetry of the system, thus enables such a many-body system to split radiative heat flux with a high contrast ratio of heat flux (up to 99:1). For graphene/SiC core–shell (GSCS) nanoparticles, graphene modifies the localized surface resonance of the SiC core, and introduces additional photon tunneling modes through changing the polarizability, resulting in that the three-body system consisting of GSCS nanoparticles shows a high thermal splitting ratio [150]. The heat splitting effect also enables the photon-mediated thermal routing with the controllable temperature distribution by the Fermi level matching [151].

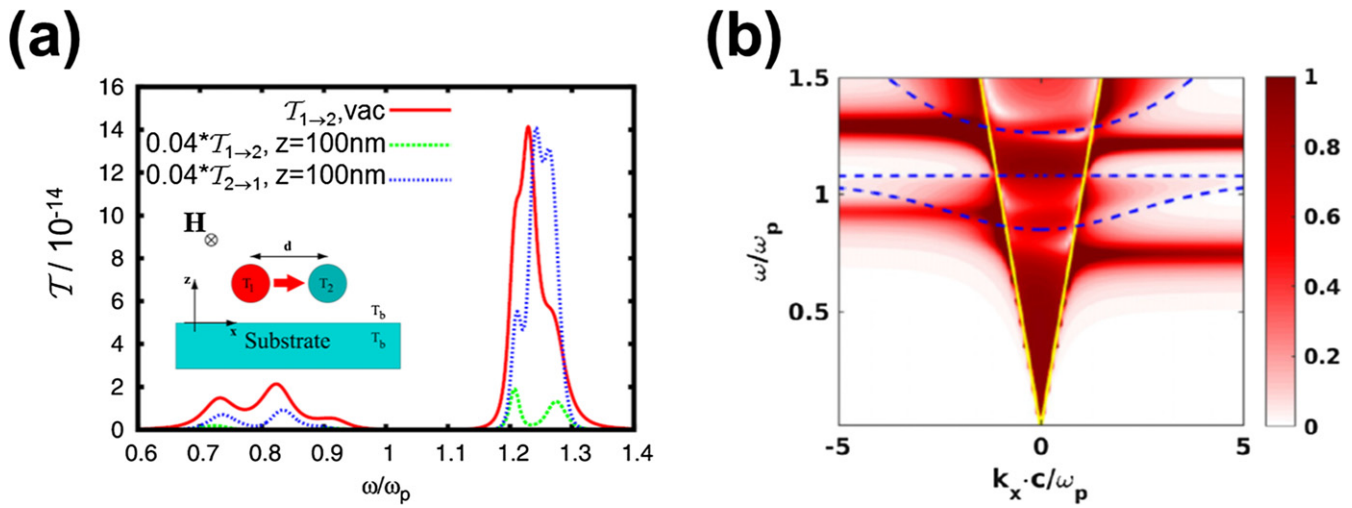

Figure 8. (a) ETCs between two InSb nanoparticles $\mathcal{T}_{1\to2}$ and $\mathcal{T}_{2\to1}$ with $H = 1$ T in vacuum (solid), and when an InSb substrate is placed from them at the distance of 100 nm (dotted, the sketch of the geometry is shown in the inset). (b) Reflection coefficient $|r_{pp}|$ for $|k_x| \leqslant k_0$ and Im $\left(r_{pp}\right)$ for $|k_x| > k_0$ ($k_y = 0$) with $H = 1$ T. The solid lines are the light lines in vacuum, and the dashed lines represent $\omega = ck_x/\sqrt{\mathrm{Re}\,(\varepsilon_3)}$. Reprinted from [77], with the permission of AIP Publishing.

4.5. Nonreciprocal thermal diode

A thermal diode mainly relies on the asymmetry of heat transport with respect to the sign of the temperature gradient, namely the difference of forward and backward heat fluxes. During the last decade, photon-mediated thermal diodes have been theoretically predicted to be enabled by dissimilar materials/structures with different temperature-dependent thermal properties via changing the temperature bias direction [152–154]. Among them, thermal diodes based on IMT materials show more remarkable rectification due to the distinct nonlinear dependence of physical properties at their phase changing temperatures, and hence attract much attention [14, 155]. However, thermal diodes mentioned above have to be naturally reciprocal according to the second law of thermodynamics. Ott *et al* [77] proposed a nonreciprocal radiative thermal diode enabled by a many-body system via applying an external magnetic field, as illustrated in figure 8(a). An InSb substrate is placed under two InSb nanoparticles, adding a magnetic field of 1 T along the y axis makes the spectral forward and backward ETCs between two InSb nanoparticles different, i.e. $\mathcal{T}_{1\to2} \neq \mathcal{T}_{2\to1}$. This directly leads to a different forward and backward heat flux between two nanoparticles, and the discrepancy shows strong dependence on the magnetic field intensity. Note that, if the InSb substrate is removed, $\mathcal{T}_{1\to2} = \mathcal{T}_{2\to1}$ for any magnetic field intensity. This nonreciprocal effect is attributed to the asymmetry with respect to the propagation direction of evanescent surface waves confined at the interfaces, according to the reflection coefficient $|r_{pp}|$ having $\omega(k_x) \neq \omega(-k_x)$ in the presence of magnetic field, as shown in figure 8(b). Using such a nonreciprocal thermal diode, the rectification efficiency of heat flux can reach to around 90% which is larger than most theoretical values reported in previous works [156–158].

4.6. Thermal transistor

Tunable RHT in two-body systems in the near-field regime has been predicted by several strategies in terms of materials including IMT materials, ferroelectric materials, semiconductors and chiral metamaterials [153, 155, 159–165]. It has been experimentally demonstrated that the rectification coefficient of heat flux between doped Si and VO_2 surfaces at ∼140 nm vacuum gap can exceed 50% [14, 20]. However, this transport mechanism only enables the RHT to be modulated in a manner of a diode which allows the heat flow to propagate preferentially in one direction, but does not enable the heat flow to be switched, modulated or amplified. The transistor, the cornerstone of practically all modern electronics, is a semiconductor device used to switch, modulate or amplify electronic signals and electrical power. The classical field-effect transistor (FET), consisting of three basic elements, the drain, the source, and the gate, is fundamentally used to control the flux of electrons. The transport mechanism is that a small variation in the voltage applied on the gate can cause a large change in the current from the source to the drain. Inspired by the FET and many-body heat transport mechanism, the near-field thermal transistor (NFTT) by using a gate (labeled by G) made of a thermally induced IMT material, i.e. VO_2 with a critical temperature $T_c = 340$ K, is theoretically proposed (see figures 9(a) and (b)) [166]. The source and the drain, labeled by the indices S and D, are made of SiO_2 which support SPhPs. Figure 9(c) shows the ETCs $\mathcal{T}_{SG}$ and $\mathcal{T}_{GD}$ when the VO_2 plate is in its insulating phase as well as the metallic phase.

When $T_G < T_c$, the gate is in its insulating phase and behaves as a uniaxial crystal with the ability to support (symmetric and antisymmetric) surface waves (see the top of figure 9(c)). The coupling of these surface waves with the SPhPs of SiO_2 leads to a high radiative heat flux, as demon-

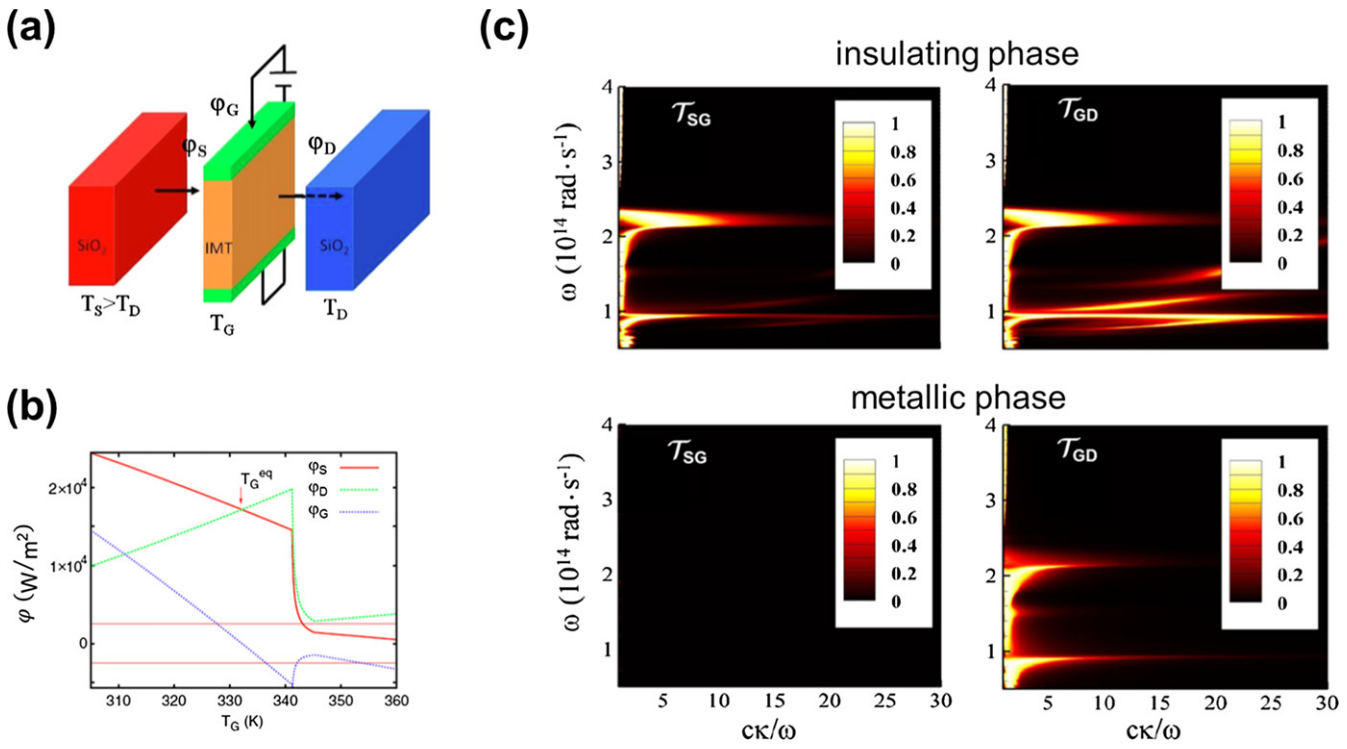

Figure 9. (a) Schematic of a NFTT. A IMT gate at the temperature T_G is located between two thermal reservoirs (source and drain) with temperatures T_S and T_D. φ_D and φ_S are the radiative heat fluxes received by the drain and emitted by the source, respectively. φ_G is the heat flux supplied to the gate to alter its temperature. (b) Operating regimes of a SiO_2–VO_2–SiO_2 NFTT. When $T_{eq,G}$ is a little bit smaller than the critical temperature T_c, a small amount of heat supplied to the gate induces a strong switching of heat fluxes φ_D and φ_S, enabling different functions of thermal switching, thermal modulation, and thermal amplification. (c) ETCs $\mathcal{T}_{SG}$ and $\mathcal{T}_{GD}$ for $\delta = 50$ nm and $d =$ 100 nm when the VO_2 plate is in its insulating phase (top) and its metallic phase (bottom). Reprinted figure with permission from [166], Copyright (2014) by the American Physical Society.

strated by the ETCs $\mathcal{T}_{SG}$ and $\mathcal{T}_{GD}$ in this case. However, when $T_G = T_c$, the gate starts to transit toward the amorphous metallic phase and remains in this state for $T_G > T_c$. In this scenario, the gate does not support surface waves any more (see the bottom of figure 9(c)), and thus screen the thermally excited waves. In this NFTT, the radiative flux received by the drain can be denoted as φ_D, and that from the source towards the gate is φ_S. Changing the flux φ_G supplied to the gate alters the temperature T_G, permitting a SiO_2–VO_2–SiO_2 NFTT to operate in different regimes based on the phase transition properties of the gate: (i) thermal switching. An increase of T_G by about 10 degrees above $T_{G,eq}$ (the equilibrium temperature of the gate, obtained by zeroing its net flux, i.e. $\varphi_G = \varphi_S - \varphi_D = 0$) reduces φ_S and φ_D by about one order of magnitude. When T_G is slightly below or above the critical temperature T_c, this heat transport mechanism enables the NFTT to operate in two modes: the 'on' mode with a large heat flux in the case of $T_G < T_c$, and the 'off' mode with a much less heat flux in the case of $T_G > T_c$. (ii) Thermal modulation. φ_G remains quite small over the temperature region around $T_{G,eq}$, and hence φ_S and φ_D can be remarkably modulated within this temperature range. (iii) Thermal amplification. Having a negative differential thermal conductance is the key for thermal amplification [137]. When T_G is far away from T_c, the amplification factor α ($\alpha = |\partial\varphi_D/\partial\varphi_G|$) of the NFTT is approximately 0.5, because the slopes of φ_S and φ_D are almost identical. However, α is larger than 1 when $T_{G,eq}$ is around T_c, demonstrating the thermal amplification when in this temperature range. Moreover, several strategies for improving the performance have been proposed. For example, patterning the intermediate VO_2 plate into 1D rectangular grating can dramatically enhance the thermal rectification ratio [167].

4.7. Thermal memory and logic gates

The temperature-dependent properties of IMT materials enable the photon-mediate heat flow to show distinct behaviors when they undergo the transition of phase states, which provide the fundamental basis of thermal logic devices for processing information by utilizing thermal photons. One of the necessary conditions to create thermophotologic devices is the radiative bistability, which only exists in many-body systems. The proposed thermal device (see figure 10(a)) consists of a SiO_2 plate on the left radiatively coupled to a low-temperature (T_L) thermal bath, and a VO_2 plate on the right coupled to a high-temperature (T_R) reservoir, while the two plates are separated by a vacuum gap. The thermal baths, serving as external blackbodies far from the rest of the system, are held at different given temperatures to enable the bistable behaviour of the IMT membrane. In order to compute the feat flux in such a many-body system, the field correlators for each body, including the thermal baths, considering the right and left scattering are employed. They take the propagating fields, related to the reflection and transmission operators of each membrane, in the regions of intracavity and all membranes into account,

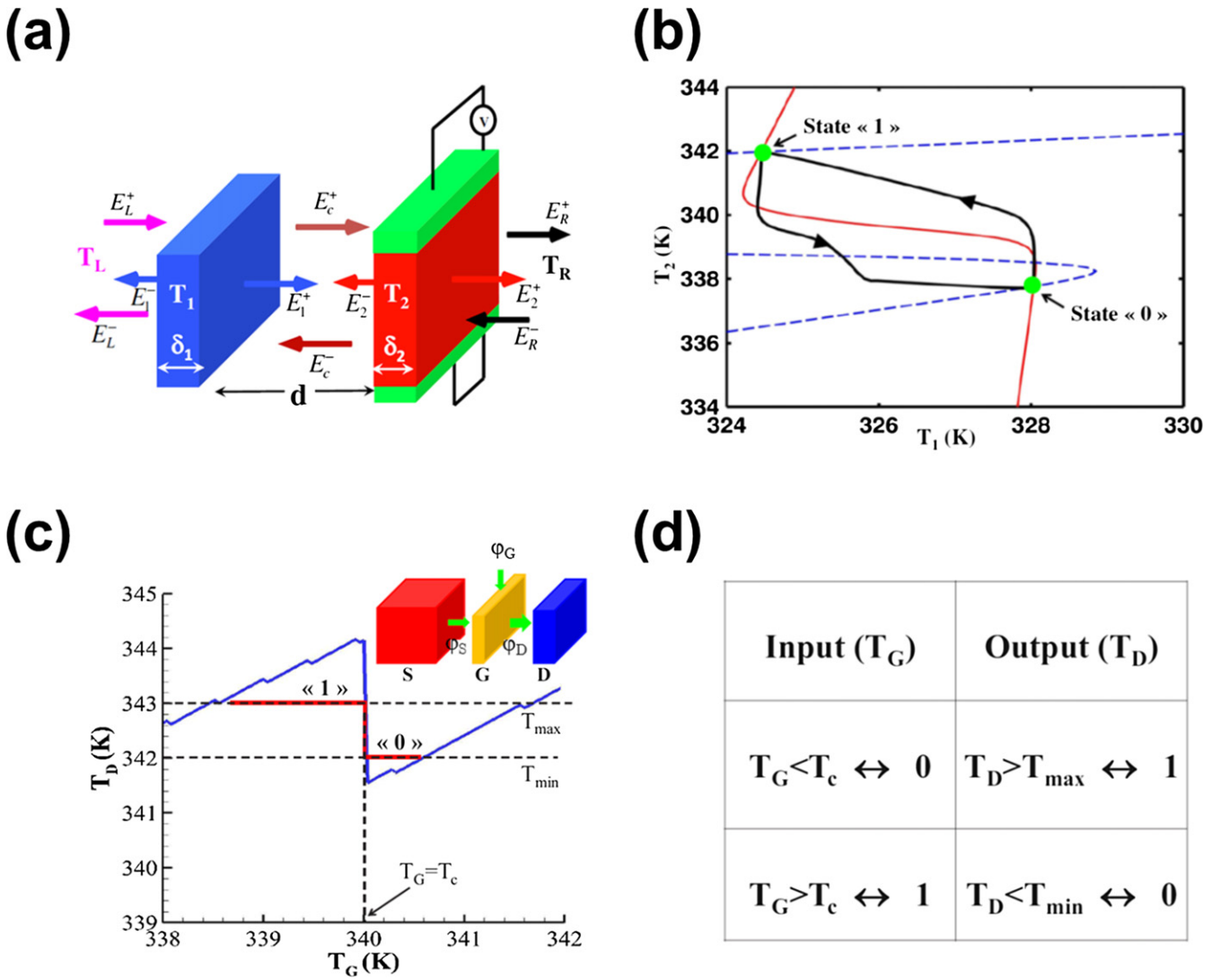

Figure 10. (a) Sketch of a radiative thermal memory device. A plate made of an IMT material is placed at a distance d from a dielectric plate. The system is surrounded by two thermal baths at different temperatures T_L and T_R. (b) The trajectory of temperatures (T_1, T_2) during the transition of system from one steady state to the other. (c) Temperature of the drain T_D as a function of the temperature of the gate T_G in the radiative NOT gate made with a SiO_2–VO_2–SiO_2 thermal transistor (see the inset). $T_{min} = 342$ K and $T_{max} = 343$ K are chosen. (d) Truth table for the NOT gate. (a), (b) Reprinted figure with permission from [168], Copyright (2014) by the American Physical Society. (c), (d) Reprinted figure with permission from [169], Copyright (2016) by the American Physical Society.

whereby the power exchanged between the system and the surrounding environment can be evaluated (see details in [85]). The thermal equilibrium state of the SiO_2–VO_2 system is characterized by a set of (T_1, T_2) where the net radiative heat flux into each plate vanish. Because VO_2 undergoes phase transition from its high-temperature metallic state to its low-temperature insulating state at 340 K, the SiO_2–VO_2 system has two stable equilibrium states (radiative bistability), termed as state '0' with $T_2 = 338$ K and state '1' with $T_2 = 342$ K, respectively, which are represented by the green dots corresponding to two phase states of VO_2. The trajectory of temperatures (T_1, T_2) illustrates how the temperatures of SiO_2–VO_2 system evolve from the initial random state to the final state. The SiO_2–VO_2 system can transit from state '0' to state '1' by adding heat into the VO_2 plate to make it transit from its insulating phase into its metallic phase. In this case, information can be stored as long as the thermal reservoirs remain active, enabling a volatile thermal memory device. To go from state '1' to state '0', the VO_2 plate needs to be cooled down to its insulating phase. To read out the thermal state of the system, proper thermometers should be used to measure the temperatures (T_1, T_2). These predictions demonstrate the existence of bistable thermal behaviors in many-body systems, and also enables such a contactless system to store thermal information for an arbitrarily long time between the phase transitions [168].

The Boolean algebra, which is usually implemented using logic gates (i.e. NOT, OR, and AND gates) by logic operations, is the fundamental theoretical framework for information processing. The concept of photonic thermal logic gates based on a SiO_2–VO_2–SiO_2 system (see figure 10(c)) is proposed. To operate the system as a NOT gate, the thermal source is fixed at T_S, and the intermediate VO_2 plate functions as the input of the NOT gate and the drain as the output. According to the radiative bistability as mentioned above, fixing T_S and

T_G, there exists a T_D which enables the radiative heat flux from the source and gate towards the drain φ_D to be zero, indicating the drain is in its thermal equilibrium and the system is under the steady state at this moment. For $T_G < T_c$, SiO_2 and VO_2 support SPhPs in the same frequency range, resulting in strong RHT and a high T_D. For $T_G > T_c$, VO_2 does not support SPhPs so that the RHT within the system is strongly reduced which leads to a lower T_D. Hence, the output temperature of the drain T_D can be read out to characterize the Boolean output of the NOT gate. According to the output temperature T_D as a function of the gate temperature T_G with setting $T_{min} = 342$ K and $T_{max} = 343$ K as shown in figure 10(c), there exists a temperature region with $T_D > T_{max}$ when $T_G < T_c$, which means that the input state '0' leads to the output state '1'. Similarly, there also exists a region where $T_D < T_{min}$ when $T_G > T_c$, which means that the input state '1' results in the output state '0'. These two regions demonstrate that the device can function as a NOT gate according to the truth table shown in figure 10(d). Furthermore, the OR and AND gates can also be realized by changing the materials in source, gate and drain. Together with the NOT gate, such a many-body system with IMT material allows for a full information treatment by Boolean operations via thermal photons [169].

5. Concluding remarks

In this review, we first briefly introduced various methods developed to quantify many-body NFRHT, including the analytical formalism, the numerical scattering matrix method, TDDA, FSC approach, FDTD, and the KT formalism. Due to the many-body effects, there are some emerging functionalities, including enhanced RHT, MO-induced heat transport, superdiffusive and ballistic heat transport, photon drag effect and collective thermal emission. Then, we discussed the enabled applications based on many-body NFRHT, including thermal waveguide, heat engine, heat pump, heat flux switch and splitter, nonreciprocal thermal diode, thermal transistor, and thermal memory and logic gates.

Since many-body NFRHT is rich in physics and becomes increasingly practical, we anticipate that it will continue to prompt theoretical and technological evolution where NFRHT plays a significant role in the future. However, despite remarkable developments in many-body NFRHT, there still exist challenges and opportunities in fundamental research and practical applications.

(a) On the theoretical side, more efficient, low-cost and flexible numerical methods are needed to compute many-body NFRHT for complicated geometries and physical properties. For example, for systems with broken time-reversal symmetry, we hold the opinion that the existing scattering matrix method should be further developed to deal with. In addition, the FDTD approach [108, 170], which has never been reported to compute many-body NFRHT, is also hopeful to be developed to handle aperiodic structures. Although the above-mentioned methods can deal with the majority of many-body cases, these methods still need mutual verification. For example, NFRHT between a cylinder and a perforated surface computed by the FSC and FDTD, has been predicted to depend nonmonotonically on their separation [171]. In many-body cases, how this anomalous NFRHT becomes and whether these methods agree with each other remain open. Furthermore, we also envision that more comprehensive exploration of many-body NFRHT combined with topological photonics and spatiotemporal modulation [172, 173] may introduce more novel heat transport mechanisms.

(b) On the experimental side, thus far, too many theoretical results and concepts are waiting for experimental verification which may revolutionize the study on NFRHT. Nevertheless, the control of interplate parallelism and distance, and the measurement of heat flux, require more precisely nanofabricated structures and become more daunting for many-body planar systems than two-body systems. For particles or other dipolar systems, it seems feasible to evaluate the RHT by highly sensitive thermometers with ultrahigh precision of temperature control on the basis of elongated microscope tips in multi-tip SThM setups which are electrostatically tuned and thermocouple-integrated individually [28, 136].

(c) In terms of practical applications, many existing concepts and functionalities in two-body systems can be expectedly extended to many-body systems with judicious design to obtain better performance of (low-grade) energy utilization, thermal management and even information technology using thermal photons [174, 175]. From the practical perspective, an integrated device using many-body NFRHT is more recommended to maintain the gap distance at the nanoscale instead of control it precisely, but there's still a long way to go for practical applications.

Note: during the submission, we noticed that recently there exists another unpublished review article on many-body NFRHT [176], which discussed the topic of NFRHT in the two-body and many-body systems in terms of heat transport regimes, equilibrium states and multistable states, and thermomagnetic effects. In our review, we only focus on many-body NFRHT, and pay more attention to the progress summary of theories, functionalities and the enabled applications in many-body systems.

Acknowledgments

This work is supported by the National Natural Science Foundation of China (Grant Nos. 51806070, 51676077, and 52076087), the Postdoctoral Research Foundation of China (Grant No. 2018M632849), the Fundamental Research Funds for the Central Universities (Grant No. 2019kfyXKJC033), and Wuhan City Science and Technology Program (2020010601012197).

Data availability statement

All data that support the findings of this study are included within the article (and any supplementary files).

ORCID iDs

Jinlin Song https://orcid.org/0000-0003-4202-9760
Qiang Cheng https://orcid.org/0000-0002-4370-2120
Run Hu https://orcid.org/0000-0003-0274-9982

References

[1] Zhang Z M 2007 *Nano/Microscale Heat Transfer* (New York: McGraw-Hill)
[2] Modest M F 2013 *Radiative Heat Transfer* (New York: Academic)
[3] Planck M 1991 *The Theory of Heat Radiation* (New York: Dover)
[4] Bohm D 1989 *Quantum Theory* (New York: Dover)
[5] Van Hove M and Polder D 1971 Theory of radiative heat transfer between closely spaced bodies *Phys. Rev.* B **4** 3303–14
[6] Rytov S M 1959 *Air Force Cambridge Research Labs* (Cambridge, MA: Hanscom Air Force Base)
[7] Hu L, Narayanaswamy A, Chen X and Chen G 2008 Near-field thermal radiation between two closely spaced glass plates exceeding Planck's blackbody radiation law *Appl. Phys. Lett.* **92** 133106
[8] Shen S, Narayanaswamy A and Chen G 2009 Surface phonon polaritons mediated energy transfer between nanoscale gaps *Nano Lett.* **9** 2909–13
[9] DeSutter J, Tang L and Francoeur M 2019 A near-field radiative heat transfer device *Nat. Nanotechnol.* **148** 751–5
[10] Kim K *et al* 2015 Radiative heat transfer in the extreme near field *Nature* **528** 387–91
[11] Shi J, Liu B, Li P, Ng L Y and Shen S 2015 Near-field energy extraction with hyperbolic metamaterials *Nano Lett.* **15** 1217–21
[12] St-Gelais R, Zhu L, Fan S and Lipson M 2016 Near-field radiative heat transfer between parallel structures in the deep subwavelength regime *Nat. Nanotechnol.* **11** 515–9
[13] Bernardi M P, Milovich D and Francoeur M 2016 Radiative heat transfer exceeding the blackbody limit between macroscale planar surfaces separated by a nanosize vacuum gap *Nat. Commun.* **7** 12900
[14] Fiorino A *et al* 2018 A thermal diode based on nanoscale thermal radiation *ACS Nano* **12** 5774–9
[15] Fiorino A, Thompson D, Zhu L, Song B, Reddy P and Meyhofer E 2018 Giant enhancement in radiative heat transfer in sub-30 nm gaps of plane parallel surfaces *Nano Lett.* **18** 3711–5
[16] Fiorino A, Zhu L, Thompson D, Mittapally R, Reddy P and Meyhofer E 2018 Nanogap near-field thermophotovoltaics *Nat. Nanotechnol.* **13** 806–11
[17] Ghashami M *et al* 2018 Precision measurement of phonon-polaritonic near-field energy transfer between macroscale planar structures under large thermal gradients *Phys. Rev. Lett.* **120** 175901
[18] Guha B, Otey C, Poitras C B, Fan S and Lipson M 2012 Near-field radiative cooling of nanostructures *Nano Lett.* **12** 4546–50
[19] Ito K, Miura A, Iizuka H and Toshiyoshi H 2015 Parallel-plate submicron gap formed by micromachined low-density pillars for near-field radiative heat transfer *Appl. Phys. Lett.* **106** 083504
[20] Ito K, Nishikawa K, Miura A, Toshiyoshi H and Iizuka H 2017 Dynamic modulation of radiative heat transfer beyond the blackbody limit *Nano Lett.* **17** 4347–53
[21] Kralik T *et al* 2012 Strong near-field enhancement of radiative heat transfer between metallic surfaces *Phys. Rev. Lett.* **109** 224302
[22] Lang S *et al* 2017 Dynamic measurement of near-field radiative heat transfer *Sci. Rep.* **7** 13916
[23] Lim M, Lee S S and Lee B J 2015 Near-field thermal radiation between doped silicon plates at nanoscale gaps *Phys. Rev.* B **91** 195136
[24] Ottens R S *et al* 2011 Near-field radiative heat transfer between macroscopic planar surfaces *Phys. Rev. Lett.* **107** 014301
[25] Shi J, Li P, Liu B and Shen S 2013 Tuning near field radiation by doped silicon *Appl. Phys. Lett.* **102** 183114
[26] Song B *et al* 2015 Enhancement of near-field radiative heat transfer using polar dielectric thin films *Nat. Nanotechnol.* **10** 253–8
[27] Song B, Thompson D, Fiorino A, Ganjeh Y, Reddy P and Meyhofer E 2016 Radiative heat conductances between dielectric and metallic parallel plates with nanoscale gaps *Nat. Nanotechnol.* **11** 509–14
[28] St-Gelais R, Guha B, Zhu L, Fan S and Lipson M 2014 Demonstration of strong near-field radiative heat transfer between integrated nanostructures *Nano Lett.* **14** 6971–5
[29] Worbes L, Hellmann D and Kittel A 2013 Enhanced near-field heat flow of a monolayer dielectric island *Phys. Rev. Lett.* **110** 134302
[30] van Zwol P J, Thiele S, Berger C, de Heer W A and Chevrier J 2012 Nanoscale radiative heat flow due to surface plasmons in graphene and doped silicon *Phys. Rev. Lett.* **109** 264301
[31] van Zwol P J, Ranno L and Chevrier J 2012 Tuning near field radiative heat flux through surface excitations with a metal insulator transition *Phys. Rev. Lett.* **108** 234301
[32] Chen K, Santhanam P and Fan S 2015 Suppressing sub-bandgap phonon-polariton heat transfer in near-field thermophotovoltaic devices for waste heat recovery *Appl. Phys. Lett.* **107** 091106
[33] Zhu L, Fiorino A, Thompson D, Mittapally R, Meyhofer E and Reddy P 2019 Near-field photonic cooling through control of the chemical potential of photons *Nature* **566** 239–44
[34] Jones A C and Raschke M B 2012 Thermal infrared near-field spectroscopy *Nano Lett.* **12** 1475–81
[35] Kittel A, Wischnath U F, Welker J, Huth O, Rüting F and Biehs S-A 2008 Near-field thermal imaging of nanostructured surfaces *Appl. Phys. Lett.* **93** 193109
[36] De Wilde Y, Formanek F, Carminati R, Gralak B, Lemoine P-A, Joulain K, Mulet J-P, Chen Y and Greffet J-J 2006 Thermal radiation scanning tunnelling microscopy *Nature* **444** 740–3
[37] Kittel A *et al* 2005 Near-field heat transfer in a scanning thermal microscope *Phys. Rev. Lett.* **95** 224301
[38] Zhao B, Chen K, Buddhiraju S, Bhatt G, Lipson M and Fan S 2017 High-performance near-field thermophotovoltaics for waste heat recovery *Nano Energy* **41** 344–50
[39] Liu X and Zhang Z M 2016 High-performance electroluminescent refrigeration enabled by photon tunneling *Nano Energy* **26** 353–9
[40] Yang Y, Sabbaghi P and Wang L 2017 Effect of magnetic polaritons in SiC deep gratings on near-field radiative transfer *Int. J. Heat Mass Transfer* **108** 851–9
[41] Yang Y and Wang L 2016 Spectrally enhancing near-field radiative transfer between metallic gratings by exciting magnetic polaritons in nanometric vacuum gaps *Phys. Rev. Lett.* **117** 044301
[42] Bai Y, Jiang Y and Liu L 2015 Enhanced near-field radiative heat transfer between a nanosphere and a hyperbolic metamaterial mediated by coupled surface phonon polaritons *J. Quant. Spectrosc. Radiat. Transfer* **158** 61–8
[43] Biehs S A, Lang S, Petrov A Y, Eich M and Ben-Abdallah P 2015 Blackbody theory for hyperbolic materials *Phys. Rev. Lett.* **115** 174301
[44] Biehs S A, Tschikin M and Ben-Abdallah P 2012 Hyperbolic metamaterials as an analog of a blackbody in the near field *Phys. Rev. Lett.* **109** 104301

[45] Biehs S-A, Tschikin M, Messina R and Ben-Abdallah P 2013 Super-Planckian near-field thermal emission with phonon-polaritonic hyperbolic metamaterials *Appl. Phys. Lett.* **102** 131106

[46] Biehs S and Ben-Abdallah P 2017 Near-field heat transfer between multilayer hyperbolic metamaterials *Z. Nat.forsch.* A **72** 115–27

[47] Bright T J, Liu X L and Zhang Z M 2014 Energy streamlines in near-field radiative heat transfer between hyperbolic metamaterials *Opt. Express* **22** A1112–27

[48] Chang J-Y, Yang Y and Wang L 2015 Tungsten nanowire based hyperbolic metamaterial emitters for near-field thermophotovoltaic applications *Int. J. Heat Mass Transfer* **87** 237–47

[49] Dai J 2017 Ultrabroadband super-Planckian radiative heat transfer with artificial continuum cavity states in patterned hyperbolic metamaterials *Phys. Rev.* B **95** 245405

[50] Guo Y, Cortes C L, Molesky S and Jacob Z 2012 Broadband super-Planckian thermal emission from hyperbolic metamaterials *Appl. Phys. Lett.* **101** 131106

[51] Ikeda T, Ito K and Iizuka H 2017 Tunable quasi-monochromatic near-field radiative heat transfer in s and p polarizations by a hyperbolic metamaterial layer *J. Appl. Phys.* **121** 013106

[52] Jin S, Lim M, Lee S S and Lee B J 2016 Hyperbolic metamaterial-based near-field thermophotovoltaic system for hundreds of nanometer vacuum gap *Opt. Express* **24** A635

[53] Liu B and Shen S 2013 Broadband near-field radiative thermal emitter/absorber based on hyperbolic metamaterials: direct numerical simulation by the Wiener chaos expansion method *Phys. Rev.* B **87** 115403

[54] Liu X L, Zhang R Z and Zhang Z M 2013 Near-field thermal radiation between hyperbolic metamaterials: graphite and carbon nanotubes *Appl. Phys. Lett.* **103** 213102

[55] Liu X L and Zhang Z M 2015 Giant enhancement of nanoscale thermal radiation based on hyperbolic graphene plasmons *Appl. Phys. Lett.* **107** 143114

[56] Liu X, Zhang R Z and Zhang Z 2014 Near-perfect photon tunneling by hybridizing graphene plasmons and hyperbolic modes *ACS Photonics* **1** 785–9

[57] Messina R, Ben-Abdallah P, Guizal B, Antezza M and Biehs S 2016 Hyperbolic waveguide for long-distance transport of near-field heat flux *Phys. Rev.* B **94** 104301

[58] Miller O D, Johnson S G and Rodriguez A W 2014 Effectiveness of thin films in lieu of hyperbolic metamaterials in the near field *Phys. Rev. Lett.* **112** 157402

[59] Tschikin M, Biehs S-A, Messina R and Ben-Abdallah P 2013 On the limits of the effective description of hyperbolic materials in the presence of surface waves *J. Opt.* **15** 105101

[60] Zhang R Z and Zhang Z M 2017 Validity of effective medium theory in multilayered hyperbolic materials *J. Quant. Spectrosc. Radiat. Transfer* **197** 132–40

[61] Song J and Cheng Q 2016 Near-field radiative heat transfer between graphene and anisotropic magneto-dielectric hyperbolic metamaterials *Phys. Rev.* B **94** 125419

[62] Ilic O, Thomas N H, Christensen T, Sherrott M C, Soljačić M, Minnich A J, Miller O D and Atwater H A 2018 Active radiative thermal switching with graphene plasmon resonators *ACS Nano* **12** 2474–81

[63] Shi K, Bao F and He S 2017 Enhanced near-field thermal radiation based on multilayer graphene-hBN heterostructures *ACS Photonics* **4** 971–8

[64] Liu X L and Zhang Z M 2014 Graphene-assisted near-field radiative heat transfer between corrugated polar materials *Appl. Phys. Lett.* **104** 251911

[65] Messina R, Ben-Abdallah P, Guizal B and Antezza M 2017 Graphene-based amplification and tuning of near-field radiative heat transfer between dissimilar polar materials *Phys. Rev.*B **96** 045402

[66] Svetovoy V B and Palasantzas G 2014 Graphene-on-Silicon near-field thermophotovoltaic cell *Phys. Rev. Appl.* **2** 034006

[67] Miller O D, Ilic O, Christensen T, Reid M T H, Atwater H A, Joannopoulos J D, Soljačić M and Johnson S G 2017 Limits to the optical response of graphene and two-dimensional materials *Nano Lett.* **17** 5408–15

[68] Zhao B, Guizal B, Zhang Z M, Fan S and Antezza M 2017 Near-field heat transfer between graphene/hBN multilayers *Phys. Rev.*B **95** 245437

[69] Zheng Z, Wang A and Xuan Y 2018 Spectral tuning of near-field radiative heat transfer by graphene-covered metasurfaces *J. Quant. Spectrosc. Radiat. Transfer* **208** 86–95

[70] Drosdoff D, Phan A D and Woods L M 2014 Transverse electric mode for near-field radiative heat transfer in graphene-metamaterial systems *Adv. Opt. Mater.* **2** 1038–42

[71] Messina R 2013 Tuning the electromagnetic local density of states in graphene-covered systems via strong coupling with graphene plasmons *Phys. Rev.* B **87** 085421

[72] Messina R, Antezza M and Ben-Abdallah P 2012 Three-body amplification of photon heat tunneling *Phys. Rev. Lett.* **109** 244302

[73] Thompson D, Zhu L, Meyhofer E and Reddy P 2020 Nanoscale radiative thermal switching via multi-body effects *Nat. Nanotechnol.* **15** 99–104

[74] Latella I and Ben-Abdallah P 2017 Giant thermal magnetoresistance in plasmonic structures *Phys. Rev. Lett.* **118** 173902

[75] Zhu L and Fan S 2016 Persistent directional current at equilibrium in nonreciprocal many-body near field electromagnetic heat transfer *Phys. Rev. Lett.* **117** 134303

[76] Ben-Abdallah P 2016 Photon thermal Hall effect *Phys. Rev. Lett.* **116** 084301

[77] Ott A, Messina R, Ben-Abdallah P and Biehs S-A 2019 Radiative thermal diode driven by nonreciprocal surface waves *Appl. Phys. Lett.* **114** 163105

[78] Cuevas J C and García-Vidal F J 2018 Radiative heat transfer *ACS Photonics* **5** 3896–915

[79] Lemons D S and Gythiel A 1997 Paul Langevin's 1908 paper 'On the theory of Brownian motion' ['Sur la théorie du mouvement brownien' *C. R. Acad. Sci. (Paris)* **146** 530–3 (1908)] *Am. J. Phys.* **65** 1079–81
Lemons D S and Gythiel A 1997 *Am. J. Phys.* **65** 1079–81

[80] Milonni P W and Shih M L 1991 Zero-point energy in early quantum theory *Am. J. Phys.* **59** 684–98

[81] Song J, Lu L, Cheng Q and Luo Z 2018 Three-body heat transfer between anisotropic magneto-dielectric hyperbolic metamaterials *J. Heat Transfer* **140** 082005

[82] Kan Y H, Zhao C Y and Zhang Z M 2019 Near-field radiative heat transfer in three-body systems with periodic structures *Phys. Rev.* B **99** 035433

[83] He M-J, Qi H, Li Y, Ren Y-T, Cai W-H and Ruan L-M 2019 Graphene-mediated near field thermostat based on three-body photon tunneling *Int. J. Heat Mass Transfer* **137** 12–9

[84] Latella I, Pérez-Madrid A, Rubi J M, Biehs S and Ben-Abdallah P 2015 Heat engine driven by photon tunneling in many-body systems *Phys. Rev. Appl.* **4** 011001

[85] Latella I, Ben-Abdallah P, Biehs S, Antezza M and Messina R 2017 Radiative heat transfer and nonequilibrium Casimir–Lifshitz force in many-body systems with planar geometry *Phys. Rev.* B **95** 205404

[86] Ben-Abdallah P, Biehs S and Joulain K 2011 Many-body radiative heat transfer theory *Phys. Rev. Lett.* **107** 114301

[87] Nikbakht M 2014 Radiative heat transfer in anisotropic many-body systems: tuning and enhancement *J. Appl. Phys.* **116** 094307

[88] Ben-Abdallah P, Belarouci A, Frechette L and Biehs S-A 2015 Heat flux splitter for near-field thermal radiation *Appl. Phys. Lett.* **107** 053109

[89] Albaladejo S, Gómez-Medina R, Froufe-Pérez L S, Marinchio H, Carminati R, Torrado J F, Armelles G, García-Martín A and Sáenz J J 2010 Radiative corrections to the polarizability tensor of an electrically small anisotropic dielectric particle *Opt. Express* **18** 3556–67

[90] Chapuis P-O, Laroche M, Volz S and Greffet J-J 2008 Radiative heat transfer between metallic nanoparticles *Appl. Phys. Lett.* **92** 201906

[91] Dong J, Zhao J and Liu L 2017 Radiative heat transfer in many-body systems: coupled electric and magnetic dipole approach *Phys. Rev.* B **95** 125411

[92] Müller B, Incardone R, Antezza M, Emig T and Krüger M 2017 Many-body heat radiation and heat transfer in the presence of a nonabsorbing background medium *Phys. Rev.*B **95** 085413

[93] Song J *et al* 2020 Magnetically tunable near-field radiative heat transfer in hyperbolic metamaterials *Phys. Rev. Appl.* **13** 024054

[94] Zhang B, Song J, Lu L, Li B, Zhou K, Cheng Q and Luo Z 2020 Magnetic-field control of near-field radiative heat transfer between graphene-based hyperbolic metamaterials *Appl. Phys. Lett.* **117** 163901

[95] Francoeur M, Pinar Mengüç M and Vaillon R 2009 Solution of near-field thermal radiation in one-dimensional layered media using dyadic Green's functions and the scattering matrix method *J. Quant. Spectrosc. Radiat. Transfer* **110** 2002–18

[96] Krüger M, Bimonte G, Emig T and Kardar M 2012 Trace formulas for nonequilibrium Casimir interactions, heat radiation, and heat transfer for arbitrary objects *Phys. Rev.*B **86** 115423

[97] Schwinger J and Lippmann B A 1950 Variational principles for scattering processes. I *Phys. Rev.* **79** 469–80

[98] Zhu L, Guo Y and Fan S 2018 Theory of many-body radiative heat transfer without the constraint of reciprocity *Phys. Rev.* B **97** 094302

[99] Chen K, Zhao B and Fan S 2018 MESH: a free electromagnetic solver for far-field and near-field radiative heat transfer for layered periodic structures *Comput. Phys. Commun.* **231** 163–72

[100] Edalatpour S and Francoeur M 2014 The thermal discrete dipole approximation (T-DDA) for near-field radiative heat transfer simulations in three-dimensional arbitrary geometries *J. Quant. Spectrosc. Radiat. Transfer* **133** 364–73

[101] Abraham Ekeroth R M, García-Martín A and Cuevas J C 2017 Thermal discrete dipole approximation for the description of thermal emission and radiative heat transfer of magneto-optical systems *Phys. Rev.* B **95** 235428

[102] Francoeur M, Cola B, Zhang Z and Tervo E 2019 Thermal radiation in systems of many dipoles *Phys. Rev.* B **100** 205422

[103] Rodriguez A W, Reid M T H and Johnson S G 2012 Fluctuating-surface-current formulation of radiative heat transfer for arbitrary geometries *Phys. Rev.* B **86** 220302

[104] Reid M T H, Johnson S G and Rodriguez A W 2013 Fluctuating-surface-current formulation of radiative heat transfer: theory and applications *Phys. Rev.* B **88** 054305

[105] Polimeridis A G 2015 Fluctuating volume-current formulation of electromagnetic fluctuations in inhomogeneous media: incandescence and luminescence in arbitrary geometries *Phys. Rev.* B **92** 134202

[106] Chandrasekhar S 1943 Stochastic problems in physics and astronomy *Rev. Mod. Phys.* **15** 1–89

[107] Kazarinov R F and Henry C H 1996 Quantum noise in photonics *Rev. Mod. Phys.* **68** 801–53

[108] Otey C R, Zhu L, Sandhu S and Fan S 2014 Fluctuational electrodynamics calculations of near-field heat transfer in non-planar geometries: a brief overview *J. Quant. Spectrosc. Radiat. Transfer* **132** 3–11

[109] Ordonez-Miranda J, Tranchant L, Gluchko S and Volz S 2015 Energy transport of surface phonon polaritons propagating along a chain of spheroidal nanoparticles *Phys. Rev.* B **92** 115409

[110] Joulain K, Drevillon J, Le Goff C and Ben-Abdallah P 2008 Heat transport through plasmonic interactions in closely spaced metallic nanoparticle chains *Phys. Rev.* B **77** 075417

[111] Ordonez-Miranda J, Tranchant L, Joulain K, Ezzahri Y, Drevillon J and Volz S 2016 Thermal energy transport in a surface phonon-polariton crystal *Phys. Rev.* B **93** 035428

[112] Tervo E J, Adewuyi O S, Hammonds J S and Cola B A 2016 High thermal conductivity in polaritonic SiO_2 nanoparticle beds *Mater. Horiz.* **3** 434–41

[113] Tervo E J, Cola B A and Zhang Z M 2020 Comparison of kinetic theory and fluctuational electrodynamics for radiative heat transfer in nanoparticle chains *J. Quant. Spectrosc. Radiat. Transfer* **246** 106947

[114] Kathmann C, Messina R, Ben-Abdallah P and Biehs S 2018 Limitations of kinetic theory to describe near-field heat exchanges in many-body systems *Phys. Rev.* B **98** 115434

[115] Pendry J B 1983 Quantum limits to the flow of information and entropy *J. Phys. A: Math. Gen.* **16** 2161–71

[116] Keller O, Xiao M and Bozhevolnyi S 1993 Configurational resonances in optical near-field microscopy: a rigorous point-dipole approach *Surf. Sci.* **280** 217–30

[117] Nikbakht M 2017 Radiative heat transfer in fractal structures *Phys. Rev.* B **96** 125436

[118] Dong J, Zhao J M and Liu L H 2017 Near-field radiative heat transfer between clusters of dielectric nanoparticles *J. Quant. Spectrosc. Radiat. Transfer* **197** 114–22

[119] Luo M, Dong J, Zhao J, Liu L and Antezza M 2019 Radiative heat transfer between metallic nanoparticle clusters in both near field and far field *Phys. Rev.* B **99** 134207

[120] Phan A D, Phan T-L and Woods L M 2013 Near-field heat transfer between gold nanoparticle arrays *J. Appl. Phys.* **114** 214306

[121] Yannopapas V and Vitanov N V 2007 Electromagnetic Green's tensor and local density of states calculations for collections of spherical scatterers *Phys. Rev.* B **75** 115124

[122] Fujimoto S 2009 Hall effect of spin waves in frustrated magnets *Phys. Rev. Lett.* **103** 047203

[123] Rikken G L J A, Wyder P and Strohm C 2005 Phenomenological evidence for the phonon Hall effect *Phys. Rev. Lett.* **95** 155901

[124] Palik E D, Kaplan R, Gammon R W, Kaplan H, Wallis R F and Quinn J J 1976 Coupled surface magnetoplasmon-optic-phonon polariton modes on InSb *Phys. Rev.* B **13** 2497–506

[125] Abraham Ekeroth R M, Ben-Abdallah P, Cuevas J C and García-Martín A 2018 Anisotropic thermal magnetoresistance for an active control of radiative heat transfer *ACS Photonics* **5** 705–10

[126] Cuevas J C and Moncada-Villa E 2020 Magnetic field effects in the near-field radiative heat transfer between planar structures *Phys. Rev.* B **101** 085411

[127] Zawadzki W 1974 Electron transport phenomena in small-gap semiconductors *Adv. Phys.* **23** 435–522

[128] Hall E H 1879 On a new action of the magnet on electric currents *Am. J. Math.* **2** 287–92

[129] Ott A, Ben-Abdallah P and Biehs S A 2018 Circular heat and momentum flux radiated by magneto-optical nanoparticles *Phys. Rev.*B **97** 205414

[130] Ben-Abdallah P *et al* 2013 Heat superdiffusion in plasmonic nanostructure networks *Phys. Rev. Lett.* **111** 174301

[131] Latella I, Biehs S, Messina R, Rodriguez A W and Ben-Abdallah P 2018 Ballistic near-field heat transport in dense many-body systems *Phys. Rev.* B **97** 035423

[132] He M-J, Qi H, Wang Y-F, Ren Y-T, Cai W-H and Ruan L-M 2019 Near-field radiative heat transfer in multilayered graphene system considering equilibrium temperature distribution *Opt. Express* **27** A953

[133] Levchenko A and Narozhny B N 2016 Coulomb drag *Rev. Mod. Phys.* **88** 025003

[134] Ben-Abdallah P 2019 Thermal photon drag in many-body systems *Phys. Rev.* B **99** 201406

[135] Tervo E, Zhang Z and Cola B 2017 Collective near-field thermal emission from polaritonic nanoparticle arrays *Phys. Rev. Mater.* **1** 015201

[136] Ben-Abdallah P 2019 Multitip near-field scanning thermal microscopy *Phys. Rev. Lett.* **123** 264301

[137] Li B, Wang L and Casati G 2006 Negative differential thermal resistance and thermal transistor *Appl. Phys. Lett.* **88** 143501

[138] Li B, Wang L and Casati G 2004 Thermal diode: rectification of heat flux *Phys. Rev. Lett.* **93** 184301

[139] Ben-Abdallah P and Biehs S-A 2015 Contactless heat flux control with photonic devices *AIP Adv.* **5** 053502

[140] Dong J, Zhao J and Liu L 2018 Long-distance near-field energy transport via propagating surface waves *Phys. Rev.* B **97** 015201

[141] Zhang Y, Antezza M, Yi H and Tan H 2019 Metasurface-mediated anisotropic radiative heat transfer between nanoparticles *Phys. Rev.* B **100** 085426

[142] Latella I, Pérez-Madrid A, Lapas L C and Miguel Rubi J 2014 Near-field thermodynamics: useful work, efficiency, and energy harvesting *J. Appl. Phys.* **115** 124307

[143] Ben-Abdallah P and Messina R 2020 Many-body near-field radiative heat pumping *Phys. Rev.* B **101** 165435

[144] Latella I, Messina R, Rubi J M and Ben-Abdallah P 2018 Radiative heat shuttling *Phys. Rev. Lett.* **121** 023903

[145] Kottos T, Fernandez-Alcazar L J, Ellis F, Shapiro B and Kottos T 2019 Adiabatic thermal radiation pumps for thermal photonics *Phys. Rev. Lett.* **123** 165901

[146] Biehs S-A, Rosa F S S and Ben-Abdallah P 2011 Modulation of near-field heat transfer between two gratings *Appl. Phys. Lett.* **98** 243102

[147] He M-J, Qi H, Ren Y-T, Zhao Y-J and Antezza M 2020 Magnetoplasmonic manipulation of nanoscale thermal radiation using twisted graphene gratings *Int. J. Heat Mass Transfer* **150** 119305

[148] He M, Qi H, Ren Y, Zhao Y and Antezza M 2020 Active control of near-field radiative heat transfer by a graphene-gratings coating-twisting method *Opt. Lett.* **45** 2914

[149] Thongrattanasiri S, Koppens F H L and Javier Garcia De Abajo F 2012 Complete optical absorption in periodically patterned graphene *Phys. Rev. Lett.* **108** 047401

[150] Song J, Cheng Q, Luo Z, Zhou X and Zhang Z 2019 Modulation and splitting of three-body radiative heat flux via graphene/SiC core–shell nanoparticles *Int. J. Heat Mass Transfer* **140** 80–7

[151] Song J, Lu L, Li B, Zhang B, Hu R, Zhou X and Cheng Q 2020 Thermal routing via near-field radiative heat transfer *Int. J. Heat Mass Transfer* **150** 119346

[152] Joulain K, Ezzahri Y, Drevillon J, Rousseau B and De Sousa Meneses D 2015 Radiative thermal rectification between SiC and SiO_2 *Opt. Express* **23** A1388

[153] Tang L and Francoeur M 2017 Photonic thermal diode enabled by surface polariton coupling in nanostructures *Opt. Express* **25** A1043

[154] Wang L P and Zhang Z M 2013 Thermal rectification enabled by near-field radiative heat transfer between intrinsic silicon and a dissimilar material *Nanoscale Microscale Thermophys. Eng.* **17** 337–48

[155] Ben-Abdallah P and Biehs S-A 2013 Phase-change radiative thermal diode *Appl. Phys. Lett.* **103** 191907

[156] Otey C R, Lau W T and Fan S 2010 Thermal rectification through vacuum *Phys. Rev. Lett.* **104** 154301

[157] Basu S and Francoeur M 2011 Maximum near-field radiative heat transfer between thin films *Appl. Phys. Lett.* **98** 243120

[158] Ordonez-Miranda J, Joulain K, De Sousa Meneses D, Ezzahri Y and Drevillon J 2017 Photonic thermal diode based on superconductors *J. Appl. Phys.* **122** 093105

[159] van Zwol P J, Joulain K, Ben-Abdallah P and Chevrier J 2011 Phonon polaritons enhance near-field thermal transfer across the phase transition of VO_2 *Phys. Rev.* B **84** 161413

[160] Yang Y, Basu S and Wang L 2013 Radiation-based near-field thermal rectification with phase transition materials *Appl. Phys. Lett.* **103** 163101

[161] Huang Y, Boriskina S V and Chen G 2014 Electrically tunable near-field radiative heat transfer via ferroelectric materials *Appl. Phys. Lett.* **105** 244102

[162] Chen K, Santhanam P and Fan S 2016 Near-field enhanced negative luminescent refrigeration *Phys. Rev. Appl.* **6** 024014

[163] Cui L, Huang Y and Wang J 2012 Near-field radiative heat transfer between chiral metamaterials *J. Appl. Phys.* **112** 084309

[164] Ghanekar A, Ji J and Zheng Y 2016 High-rectification near-field thermal diode using phase change periodic nanostructure *Appl. Phys. Lett.* **109** 123106

[165] Chen K, Xiao T P, Santhanam P, Yablonovitch E and Fan S 2017 High-performance near-field electroluminescent refrigeration device consisting of a GaAs light emitting diode and a Si photovoltaic cell *J. Appl. Phys.* **122** 143104

[166] Ben-Abdallah P and Biehs S A 2014 Near-field thermal transistor *Phys. Rev. Lett.* **112** 044301

[167] Ghanekar A, Tian Y, Ricci M, Zhang S, Gregory O and Zheng Y 2018 Near-field thermal rectification devices using phase change periodic nanostructure *Opt. Express* **26** A209–18

[168] Kubytskyi V, Biehs S and Ben-Abdallah P 2014 Radiative bistability and thermal memory *Phys. Rev. Lett.* **113** 074301

[169] Ben-Abdallah P and Biehs S 2016 Towards Boolean operations with thermal photons *Phys. Rev.* B **94** 241401

[170] Didari A and Mengüç M P 2014 Analysis of near-field radiation transfer within nano-gaps using FDTD method *J. Quant. Spectrosc. Radiat. Transfer* **146** 214–26

[171] Rodriguez A W *et al* 2013 Anomalous near-field heat transfer between a cylinder and a perforated surface *Phys. Rev. Lett.* **110** 014301

[172] Yap H H, Ren J, Wang J and Tang G 2019 Anomalous near-field heat transfer in carbon-based nanostructures with edge states *Phys. Rev. Appl.* **11** 031004

[173] Buddhiraju S, Li W and Fan S 2020 Photonic refrigeration from time-modulated thermal emission *Phys. Rev. Lett.* **124** 077402

[174] Ordonez-Miranda J, Ezzahri Y, Tiburcio-Moreno J A, Joulain K and Drevillon J 2019 Radiative thermal memristor *Phys. Rev. Lett.* **123** 025901

[175] Zhao B, Santhanam P, Chen K, Buddhiraju S and Fan S 2018 Near-field thermophotonic systems for low-grade waste-heat recovery *Nano Lett.* **18** 5224–30

[176] Biehs S *et al* 2020 Near-field radiative heat transfer in many-body systems (arXiv:2007.05604)